Full title: Eye-specific differences in active zone addition during synaptic competition in the developing visual system

Short title: Active zone clustering during eye-specific synaptic competition

Author list: Chenghang Zhang[1], Tarlan Vatan[1], and Colenso M. Speer[1,*]

Author Affiliations: [1] Department of Biology, University of Maryland, College Park, Maryland, USA 20742.

[*]Corresponding author

E-mail: cspeer@umd.edu

Abstract

Spatially clustered synaptic inputs enable local dendritic computations important for learning, memory, and sensory processing. In the mammalian visual system, individual retinal ganglion cell (RGC) axons form clustered terminal boutons containing multiple active zones onto relay cell dendrites in the dorsal lateral geniculate nucleus (dLGN). This mature architecture arises through the addition of release sites, which strengthens selected afferents while weaker inputs are pruned. Following eye-opening, spontaneous activity and visual experience promote synaptic refinement and bouton clustering after binocular inputs have segregated. However, anatomical changes in release site addition and spatial patterning during earlier stages of eye-specific competition are not well understood. To investigate this, we examined the spatial organization of eye-specific active zones in wild type mice and a mutant line with disrupted cholinergic retinal waves. Using volumetric super-resolution single-molecule localization microscopy and electron microscopy, we found that individual retinogeniculate boutons begin forming multiple nearby presynaptic active zones during the first postnatal week. Both eyes generate these “multi-active-zone” (mAZ) inputs throughout refinement, but the dominant-eye forms more numerous mAZ contacts, each with more active zones and larger vesicle pools. At the height of competition (postnatal day 4), the non-dominant-eye projection adds many single active zone (sAZ) synapses. Mutants with abnormal cholinergic retinal waves still form mAZ inputs, but develop fewer synapses overall and show reduced synaptic clustering in projections from both eyes. Together, these findings reveal eye-specific differences in release site addition that correlate with axonal refinement outcomes during retinogeniculate refinement.

Introduction

A key mechanism for neuronal signal processing is the formation of spatially clustered synapses that facilitate local computations within individual dendrites [1-3]. Through biophysical signal integration mechanisms, neighboring synaptic inputs play critical computational roles in learning, memory, and sensory processing underlying cognition and behavior [4-7]. During circuit development, both spontaneous and sensory-driven neural activity regulate synaptic clustering, stabilizing some synapses and eliminating others to establish mature connectivity patterns [6-8].

The refinement of retinal inputs to the dorsal lateral geniculate nucleus (dLGN) of the thalamus is a model example of activity-dependent synaptic clustering [9]. Over development, boutons within the terminal arbors of individual retinogeniculate axons cluster progressively [10-13], creating multiple synaptic contacts onto individual postsynaptic targets [14-16]. Concurrently, developing RGC boutons add presynaptic release sites such that some mature retinogeniculate terminals contain several dozen active zones (AZs) [16, 17]. The formation of clustered boutons with multiple release sites subserves a critical “driver” function of retinogeniculate input [18, 19].

Retinogeniculate bouton clustering depends on visual experience, and dark-rearing after eye-opening reduces clustering within individual axon arbors [12]. However, less is known about synaptic spatial relationships and activity-dependent release site

refinement during eye-specific competition before eye-opening. During early axon ingrowth, individual RGCs extend sparse side branches in the incorrect eye-specific territory [20-22]. These transient branches form synapses that contain fewer presynaptic vesicles than those made by the same axon in the correct eye-specific domain [23]. Functional recordings after eye-opening show that while many RGC inputs are pruned, the remaining inputs strengthen by adding release sites [24]. This leads to glutamate spillover and cross talk between RGC inputs that increases postsynaptic relay neuron excitability [25]. Thus, early eye-specific differences in release site number or spacing may contribute to binocular input refinement prior to eye-opening.

In a previous study from our laboratory, we used volumetric stochastic optical reconstruction microscopy (STORM), anterograde tract tracing, and immunohistochemical labeling of synaptic proteins to show that dominant-eye synapses contain more total vesicles and have more vesicles near the AZ (putative docking) compared with non-dominant-eye synapses [26]. However, we did not examine whether eye-specific inputs differ in AZ number or AZ spatial proximity (clustering) during synaptic competition. To address this gap, we reanalyzed our published dataset, focusing on eye-specific AZ spatial relationships. We found that projections from each eye form a subset of retinogeniculate inputs in which several (2-4) AZs share a common cluster of presynaptic vesicles. We refer to these synapses as multi-active-zone (mAZ) inputs. All other retinogeniculate inputs contained one single active zone and its associated vesicle cluster, and we term these single-active-zone (sAZ) synapses.

During eye-specific synaptic competition, the dominant-eye projection formed more mAZ inputs, each with more AZs and a larger presynaptic vesicle pool compared to the non-dominant eye projection. Similarly, the dominant-eye had higher vesicle signal at sAZ inputs. At the peak of synaptic competition midway through the first postnatal week (postnatal day 4), the non-dominant-eye formed numerous sAZ inputs, equalizing the global synapse density between the two eyes. These eye-specific AZ patterns were disrupted in a mutant mouse line with abnormal stage II cholinergic retinal waves and retinogeniculate segregation defects.

Results

Retinogeniculate inputs form multiple active zones during eye-specific competition

To investigate active zone refinement during eye-specific segregation, we reanalyzed a volumetric super-resolution imaging dataset previously published by our laboratory [26]. We used volumetric STochastic Optical Reconstruction Microscopy (STORM) [27] to image the dLGNs of wild-type (WT) mice at three postnatal ages (P2, P4, and P8) (Fig. 1A). We labeled eye-specific inputs by monocular injection of Alexa Fluor-conjugated cholera toxin subunit B tracer (CTB) together with immunostaining for presynaptic Bassoon, postsynaptic Homer1, and presynaptic vesicular glutamate transporter 2 (VGluT2) proteins (Fig. 1B). We collected separate image volumes (~45K μm^3 each) from three biological replicates at each age. To assess the impact of spontaneous retinal activity on synaptic development across the same time period, we performed identical experiments in β2-knockout (β2KO) mice lacking the beta 2 subunit of the

nicotinic acetylcholine receptor, a mutation that disrupts spontaneous cholinergic retinal wave activity, eye-specific segregation, and retinogeniculate synapse development [22, 26, 28-36] (Fig. 1A). Because eye-specific segregation is incomplete until ~P8, we limited our re-analysis to the future contralateral eye-specific region of the dLGN, which is reliably identified across all stages of postnatal development (Fig. 1A, see also Materials and Methods).

By analyzing synapses in the contralateral dLGN from eighteen mice across three ages and two genotypes (Table S1), STORM revealed two classes of retinogeniculate inputs distinguished by active zone (AZ) number (Fig. 1B). We defined each retinogeniculate input as a single contiguous VGluT2 cluster together with all its associated presynaptic (Bassoon) and postsynaptic (Homer1) paired synaptic labels. Using this definition, inputs that had multiple (2-4) Bassoon AZs were classified as multi-active-zone (mAZ) inputs, while those with a single Bassoon AZ were designated single-active-zone (sAZ) inputs (Fig. 1B). Most mAZ inputs contained two AZs (~70-90%, varying with age, genotype, and eye-of-origin); smaller proportions contained three AZs (~10-20%) or four or more AZs (<5%) (Table S1).

Each mAZ input could be a single terminal bouton with several AZs, or a cluster of sAZ synapses within separate boutons [10, 11, 15, 16, 37]. To address this, we used electron microscopy (EM) to image retinogeniculate terminals in the dLGN at P8. We generated a transgenic line expressing mitochondrial matrix-targeted dimeric dAPEX2 reporter [38] in ipsilaterally-projecting RGCs [39-41], providing unambiguous mitochondrial labeling in

ipsiRGC axons. EM images confirmed the presence of individual retinogeniculate boutons with multiple active zones, consistent with our STORM data (Fig. 1C). Previous EM reconstructions of retinogeniculate inputs reported no evidence of RGC bouton convergence at the end of the first postnatal week [11]. Together, these results suggest that mAZ inputs in STORM images are single RGC terminals that house several closely spaced release sites. Hereafter, we use the word “synapse” only to refer to each partnered active zone (Bassoon/Homer1 pairs); mAZ inputs contain several synapses, while each sAZ input is one synapse.

Changes in eye-specific input density during synaptic competition

In our previous analysis, we reported global eye-specific synapse densities that reflected the combined mAZ and sAZ inputs. Dominant-eye synapse density was greater than that of the non-dominant eye at P2 and P8, but eye-specific synapse densities were equivalent at P4 during the peak of synaptic competition [26]. To determine how these two input classes evolve during competition, we quantified the densities and percentages of mAZ and sAZ inputs in WT and β2KO mice (Fig. 2A). Eye-of-origin for each retinogeniculate input was assigned by colocalizing CTB signal with VGluT2 (Fig. 2B). Binocular CTB control injections showed that anterograde tracing labeled >97% of retinogeniculate synapses at P4 and P8, ensuring accurate eye-specific assignment [26]. Within the contralateral eye-specific region of the dLGN, CTB(+) VGluT2 clusters were classified as “dominant-eye” inputs and CTB(-) VGluT2 clusters as “non-dominant eye” inputs (Fig. 2B).

After false discovery rate (FDR) correction for multiple comparisons within each age and genotype (see Quantification and Statistical Analysis; p(adj) values shown in all figures and Table S2), we found that the density of CTB(+) mAZ inputs tended to be higher than CTB(-) mAZ inputs in WT mice (Fig. 2C, top left). Consistent with this trend, the mAZ input fraction (% of all inputs) was significantly higher for CTB(+) dominant-eye inputs at P4 and P8 (Fig. S1, top). β2KO mice also developed differences in mAZ input density favoring the dominant-eye (Fig. 2C, bottom left; Fig. S1, bottom). For WT sAZ synapses, the dominant-eye had a significantly higher synapse density at P2 [p(adj)=0.026, Cohen's d = 5.31] and trended higher at P8 [p(adj)=0.072, Cohen's d = 2.73]. At P4, however, sAZ synapse density was equivalent between the eyes (Fig. 2C, top right; Table S2/S3). This pattern resulted from non-dominant eye sAZ synapse addition, which equalized the global input density between the eyes at P4 as we reported previously (5/95% confidence interval, -0.014-0.011 synapses / μm^3). In β2KO mice at P4, the non-dominant eye formed fewer sAZ synapses (Fig. 2C, bottom right; see Tables S2/S3). Thus, β2KO mice with disrupted retinal activity maintain a higher mAZ input fraction in the dominant-eye projection, but sAZ synapse addition is reduced at the peak of competition.

Multi- and single-active-zone inputs from the dominant eye show increased vesicle pool size and vesicle proximity to the active zone

We previously reported a dominant-eye bias in VGluT2 volume when considering all retinogeniculate inputs [26]. Here, we assessed presynaptic maturation separately in sAZ and mAZ inputs by measuring their total VGluT2 volume. In WT mice, both mAZ (Fig. 3A, left) and sAZ (Fig. 3B, left) inputs showed significant eye-specific volume differences in the middle of eye-specific competition at P4. At this age in WT mice, the median VGluT2 cluster volume in dominant-eye mAZ inputs was ~3.55 ± 1.3 μm^3 larger (mean ± S.E.) than that of non-dominant-eye inputs (Fig. 3A, left). In contrast, β2KO mice showed a smaller ~1.9 ± 1.1 μm^3 (mean ± S.E.) volume difference between median eye-specific mAZ inputs at the same age (Fig. 3A, right panel). For sAZ synapses at P4, the magnitudes of eye-specific differences in median VGluT2 volume (mean ± S.E.) were ~2.1 ± 1.0 μm^3 in WT (Fig. 3B, left) and ~1.5 ± 1.1 in β2KO mice (Fig. 3B, right). Thus, both mAZ and sAZ vesicle pool volumes are larger for the dominant eye, with the largest eye-specific differences seen for mAZ inputs in WT mice (see Table S3).

In addition to total vesicle pool volume, we quantified the readily releasable pool by measuring VGluT2 volume within a 70 nm shell around each AZ, considering this a proxy for docked vesicles (Fig. S2A-C) [26]. In WT mice at P4, dominant-eye inputs showed greater vesicle volume per AZ than non-dominant inputs, in both mAZ and sAZ terminals (Fig. S2B, left; Table S3). These eye-specific differences were absent in β2KO mice (Fig. S2B, right; Table S3). However, when comparing mAZ and sAZ inputs from the same eye, vesicle volume per AZ was similar across all ages and genotypes (Fig. S2A-C; Table S2). This confirms our previous finding that vesicle docking favors the

dominant-eye [26] and shows that AZs formed by a single eye have similar docking levels in both their mAZ and sAZ terminals.

Vesicle pool size scales with active zone number

Because mAZ inputs showed greater total VGluT2 volume than sAZ synapses, yet exhibited comparable vesicle docking, the disparity could reflect a scaling effect of vesicle pool size with increased AZ number. To evaluate how presynaptic vesicle pool volume scales with AZ number, we compared the Bassoon cluster number to VGluT2 volume for every retinogeniculate input. In both WT (Fig. S2D) and β2KO mice (Fig. S2E), mAZ inputs contained an average of 2-3 Bassoon clusters (separate AZs) in the first postnatal week. In WT mice, CTB(+) dominant-eye mAZ inputs contained more AZs than CTB(-) non-dominant-eye mAZ inputs at P4 and P8 (Fig. S2D). This maturation was delayed until P8 in β2KO mice (Fig. S2E). For CTB(+) dominant-eye inputs in both genotypes at P4, vesicle pool volume correlated positively with AZ number (Fig. 3C; Pearson correlation coefficients: WT [0.99] and β2KO [0.95]). A similar, but weaker correlation was observed for CTB(-) non-dominant-eye inputs (Pearson correlation coefficients: WT [0.97] and β2KO [0.90]. Dividing the total presynaptic VGluT2 volume by the AZ number revealed a consistent vesicle volume per AZ for both sAZ and mAZ inputs (Fig. 3D/S3, Table S3). Collectively, these results indicate that presynaptic vesicle pool volume scales with AZ number for each eye-specific input, while a dominant-eye bias persists throughout development.

Synapse clustering before eye-opening

Eye-specific competition is thought to involve stabilization of co-active, neighboring inputs from the same eye and elimination of out of sync inputs from the opposite eye [42-44]. Because axon refinement depends on the relative strength of neurotransmission between competing inputs [39, 45-51], mAZ inputs with multiple release sites could help stabilize nearby like-eye inputs [48, 52-54].

To quantify synaptic clustering patterns, we measured the distance from every eye-specific sAZ synapse to all other sAZ and mAZ inputs within each image field. sAZ synapses were often found nearby other inputs from the same eye (Fig. 4A). To define clustering, we searched volumetrically around each mAZ input and measured the fraction of sAZ synapses that were nearby at increasing distances (Fig. S4A/B). We then compared the observed percentages with datasets in which sAZ synapse positions were randomly shuffled within each neuropil volume. The largest differences occurred within a 1-2 μm search distance (Fig. S4A/B), and so we chose a 1.5 μm cutoff from the edge of each mAZ input to designate it “clustered” if at least one neighboring sAZ synapse lay within this distance and “isolated” if none did (Fig. 4B). No significant clustering was detected when sAZ and mAZ inputs originated from opposite eyes (Fig. S4C/D).

At the peak of competition in WT mice (P4), more than 65% of both mAZ and sAZ inputs were clustered for both eyes, while this proportion fell to ~50% in β2KO mice (Fig. 4B). In the WT dominant-eye projection, the fractions of clustered mAZ and sAZ inputs were similar at each age (Fig. 4C, top left panel). For the non-dominant eye projection,

however, there were slightly more clustered mAZ inputs compared to clustered sAZ inputs at P4 (Fig. 4C, bottom left panel), the age when this eye adds sAZ synapses (Fig. 2C). β2KO mice showed no difference between mAZ and sAZ clustering at any age (Fig. 4C, right panels). Additionally, in WT mice at P4 and P8, clustered mAZ inputs from both eyes had marginally more neighboring sAZ synapses than did clustered sAZ synapses (Fig. 4D, left); this enrichment was absent in β2KO mice (Fig. 4D, right). Thus, while most retinogeniculate synapses lie within 1.5 μm of another like-eye input, WT mice show a tendency toward forming more synapses near mAZ inputs during synaptic competition.

Clustered mAZ inputs in P4 WT mice were also closer together than isolated mAZ inputs. Clustered mAZ inputs formed by the dominant-eye were ~32% closer to the nearest like-eye clustered mAZ input compared to isolated mAZ inputs (Fig. 5A, left panel). In the non-dominant eye projection, clustered mAZ inputs were ~55% closer together compared to isolated mAZ inputs (Fig. 5B, left panel). Once segregation was complete at P8, distances between clustered and isolated mAZ inputs were more similar (Fig. S5). In β2KO mice, distances between isolated and clustered mAZ inputs and their nearest clustered mAZ neighbor did not differ for either eye at P4 or P8 (Fig. 5/S5, right panels). These patterns are consistent with sAZ synapse addition when mAZ inputs are in close proximity during competition.

Finally, we tested whether sAZ vesicle pool volume varies with distance to mAZ inputs. We classified each sAZ as “near” (≤1.5 μm) or “far” (>1.5 μm) relative to the nearest

like-eye mAZ input. Across ages and genotypes, vesicle pool volume was similar for near and far sAZ synapses in both eyes (Fig. S6). Thus, vesicle pool size in sAZ synapses appears independent of their proximity to mAZ inputs.

Discussion

Spontaneous retinal activity guides eye-specific refinement by strengthening dominant eye inputs in the correct territory and pruning weaker inputs from the competing eye. Using volumetric super-resolution microscopy and eye-specific synaptic immunolabeling, we previously identified activity-dependent, eye-specific differences in presynaptic vesicle pool size and vesicle association with the active zone (AZ), both favoring the dominant eye during synaptic competition [26]. Here, we reanalyzed this dataset to measure synaptic spatial arrangements during normal development and how these are affected in a mutant model with abnormal eye-specific segregation.

Early input maturation and addition of release sites

Before eye-opening, retinal ganglion cell (RGC) axons from both eyes formed terminals with either multiple active zones (mAZ inputs) or a single active zone (sAZ synapses). Electron microscopy of dAPEX2-labeled ipsilateral RGC inputs revealed individual boutons with multiple active zones. Prior electron microscopy studies in mice showed no clustering from neighboring RGC boutons at postnatal day 8 [10, 11], suggesting the mAZ inputs seen in STORM images are single boutons containing multiple release sites. During competition, the dominant eye projection generated more of these mAZ inputs, each with more active zones and larger vesicle pools than the non-dominant eye. We

observed a linear relationship between presynaptic vesicle signal volume and active zone number, suggesting that release site addition and vesicle pool expansion may be linked during input maturation. Functional recordings indicate that release site addition is the primary driver of retinogeniculate input strengthening after eye-opening [24]. Our findings reveal that eye-specific differences in release site addition at individual terminals emerge at the earliest stages of binocular refinement.

Spatial interactions during competition

Ipsilateral RGC axons are delayed in entering the dLGN until after contralateral inputs have already innervated the nucleus [55]. Despite their late arrival, these axons competed by forming numerous sAZ inputs, which equalized the overall input density between the eyes in the future contralateral eye domain at postnatal day 4 (P4). Most of these synapses formed nearby other like-eye neighbors, and were enriched near mAZ inputs, supporting the idea of release site addition at strong synapses. Neighboring sAZ synapses could ultimately mature into mAZ inputs as release sites are added and vesicle pools expand.

Distance analysis showed that clustered mAZ boutons were closer together than isolated mAZ boutons, further supporting release site addition near strong neighboring inputs. It remains unknown, however, whether nearby mAZ inputs originate from the same RGC. Nearby mAZ inputs within individual RGC arbors could promote release site addition via intrinsic mechanisms that scale with release site number, such as increased presynaptic calcium entry or surface delivery of synaptogenic molecules via presynaptic

release. Boutons with multiple release sites could also trigger non-cell-autonomous signaling mechanisms that stabilize neighboring inputs from the same eye [48, 53, 54]. Release site addition increases extracellular glutamate concentration and promotes spillover onto adjacent synapses, which enhances the excitability of developing relay cells [25] and could contribute to long term synaptic plasticity evoked by high frequency spiking in retinal wave bursts [56-59]. Consequently, release site addition and local bouton clustering may act in tandem to stabilize coactive inputs.

Competitive refinement also involves synapse elimination and axonal retraction through punishment signals. Genetic deletions of VGluT2 or RIM1 proteins in ipsilaterally-projecting RGCs decreased presynaptic vesicle release and prevented retraction of contralateral RGC axons from the ipsilateral territory [39, 45]. One downstream mediator of synaptic punishment is JAK2 kinase, which is phosphorylated in less active synapses [52]. Similar to neurotransmission mutant phenotypes, disruption of JAK2 signaling prevents axon retraction (punishment) during competition [52]. The spatial analyses we developed here will enable future mapping of input-specific punishment signals during synaptic competition. This includes phospho-JAK2 as well as molecular tags for glial pruning of weak inputs during eye-specific segregation [60-62].

Requirement for spontaneous retinal activity

β2KO mice showed significant defects in synapse addition during the first postnatal week. mAZs still formed with similar overall ratios as in wild type controls (Fig. S1, Table S3) and eye-specific differences in vesicle pool size still emerged. However, β2KO mice

failed to form many sAZ synapses at the height of competition (P4), particularly in the late-arriving non-dominant (ipsilateral) eye projection. The failure to add synapses could explain the observation that synaptic clustering was reduced and more inputs formed in isolation in the mutants compared to controls.

While our results highlight developmental changes in presynaptic release site addition and clustering, activity-dependent postsynaptic mechanisms also influence input refinement at later stages. Retinogeniculate synapses undergo postsynaptic strengthening and weakening through potentiation and depression mediated by AMPARs and NMDARs [56-59]. After eye-specific segregation, spontaneous retinal activity is required for postsynaptic AMPAR insertion, synaptic strengthening, and elimination of weaker inputs [63]. Continued maintenance of segregation depends on calcium influx into relay neurons via L-type calcium channels, further implicating postsynaptic signaling in late-stage refinement [64, 65]. Input targeting may also be guided by molecular cues to form non-random, eye-specific connections with postsynaptic targets. Ipsilaterally-projecting RGCs have distinct gene expression profiles that specify axon guidance and may further support eye-specific synaptic targeting [66, 67]. Spontaneous retinal activity may permit axons to read out molecular regulators of synaptogenesis, as previously shown for RGC axon retraction [68].

Release site addition as a general mechanism underlying synaptic competition

Early synaptic clustering during retinogeniculate development resembles other circuits where neural activity guides competitive synaptic and axonal remodeling. At the

neuromuscular junction (NMJ), motor neuron terminals compete for control of a postsynaptic muscle fiber; a single motor axon input strengthens while competing axons are eliminated [69-71]. Competition at the NMJ depends on inter-synaptic distance, with motor axons losing connections located near stronger competing synapses [69, 70]. As winning terminals are enlarged, presynaptic release site addition maintains a consistent density of Bassoon clusters (~2-3/μm^2) [72]. Neighboring inputs with weaker synaptic transmission are selectively eliminated [73, 74]. Competing motor axons differ in their release probabilities early in development [75], suggesting that presynaptic efficacy triggers local “stabilization” signals in winners and “punishment” signals in losers [76]. Presynaptic agrin release stabilizes postsynaptic receptor clusters by counteracting the destabilizing, dispersal effects of acetylcholine release, emphasizing the importance of early presynaptic transmission in postsynaptic stabilization [77, 78].

Similarly, in the developing cerebellum, Purkinje cells initially receive inputs from multiple climbing fibers (CFs) during the first postnatal week. Subsequently, one winning CF emerges and consolidates its synaptic inputs, while losing CFs are pruned [79, 80]. Here again, the winning input strengthens by adding presynaptic release sites, which increases multivesicular release and elevates glutamate concentration in the synaptic cleft [81-83]. Postsynaptic ultrastructural and molecular changes occur several days later as dominant CF inputs potentiate and losing CF inputs depress [82, 84, 85] through spike-timing dependent remodeling [86, 87]. Across these models, the earliest distinguishing feature between competing inputs is relative presynaptic transmission strength. Thus,

release-site addition may be a conserved mechanism that biases synaptic refinement outcomes across developing neural circuits.

Materials and methods:

The raw imaging data in this paper were previously reported [26]. Materials and methods below are adapted from this work. All Matlab and Python code used in the work is available on GitHub (https://github.com/SpeerLab). Raw STORM images of the full data are available on the open-access Brain Imaging Library [88]. These images can be accessed here: https://doi.brainimagelibrary.org/doi/10.35077/g.1164.

Animals

Wild-type C57BL/6J mice (Stock Number 000664) and APEX2 mice (Stock Number 032764) used in this study were purchased from the Jackson Laboratory. ET33^{Cre} mice and β2KO were generously gifted by Drs. Eric M. Ullian (University of California, San Francisco) and Michael C. Crair (Yale School of Medicine), respectively. All experimental procedures were performed in accordance with an animal study protocol approved by the Institutional Animal Care and Use Committee (IACUC) at the University of Maryland. Neonatal male and female mice were used interchangeably for all experiments. Tissue from biological replicates (N=3 animals) was collected for each age (P2/P4/P8) from each genotype (WT and β2KO) (18 animals total). Primers used for genotyping β2KO mice are: forward: CAGGCGTTATCCACAAAGACAGA; reverse: TTGAGGGGAGCAGAACAGAATC; mutant reverse: ACTTGGGTTTGGGCGTGTTGAG.

Primers used for genotyping ET33Cre mice are: Forward: GGTCCTTGGCAGATGGGCAT; reverse: CGGCAAACGGACAGAAGCATT.

Electron microscopy tissue preparation

Animals were deeply anesthetized with ketamine/xylazine and transcardially perfused with 5-10 mls of 37°C 0.9% sterile saline (pH 7.2) followed by 20-30 mls of 37°C 4% EM-Grade paraformaldehyde (PFA, Electron Microscopy Sciences), 2% EM-Grade glutaraldehyde (GA, Electron Microscopy Sciences), 4mM calcium chloride ($CaCl_2$, Sigma-Aldrich) in 0.2M cacodylate buffer (pH 7.4). Brains were postfixed in the same perfusion fixative solution overnight at 4°C. Brains were vibratome sectioned in 0.2M cacodylate buffer (pH 7.4) at 100 µm. A circular tissue punch (~500 µm diameter) containing the dLGN was microdissected from each section using a blunt-end needle. dLGN sections were washed in 0.2M cacodylate buffer (pH 7.4) at 4°C on a rotator (4x 20 minutes each). Sections were incubated in 20mM glycine (Sigma-Aldrich) in 0.2M cacodylate buffer (pH 7.4) at 4°C on a rotator for 30 minutes, followed by 5 x 20 minutes washes in 0.2M cacodylate buffer (pH 7.4) at 4°C on a rotator. dLGN sections were immersed in 0.5mg/mL DAB solution, covered with foil, for 30 minutes at 4°C on a rotator. 10 µL of 0.03% hydrogen peroxide (Sigma-Aldrich) was mixed into the DAB solution (1 mL) and incubated for 10 minutes at 4°C on a rotator (light protected). The reaction was quenched with 0.2M cacodylate buffer (pH 7.4) washes (3 x 1-minute washes followed by 2 x 20 minutes washes).

Tissue preparation for scanning electron microscopy

dLGN sections were fixed in 2% osmium tetroxide (Electron Microscopy Sciences) in 0.15M cacodylate buffer (pH 7.4) for 45 minutes at room temperature. Sections were reduced with 2.5% potassium ferricyanide (Electron Microscopy Sciences) in 0.15M cacodylate buffer (pH 7.4) for 45 minutes at room temperature in the dark, followed by 2 x 10-minute washes in double distilled water. Sections were incubated in 1% aqueous thiocarbohydrazide (Electron Microscopy Sciences) for 20 minutes, followed by 2 x 10-minute washes in double distilled water. Samples were fixed in 1% aqueous osmium tetroxide for 45 minutes at room temperature, followed by 2 x 10-minute washes in double distilled water. Sections were postfixed in 1% uranyl acetate (Electron Microscopy Sciences) in 25% ethanol in the dark for 20 minutes at room temperature and washed and stored in double distilled water overnight. The next day, samples were stained with aqueous lead aspartate at 60°C for 30 minutes and washed with double distilled water 2 x 10 minutes. Tissues were dehydrated in a graded dilution series of 100% ethanol (35%; 50%; 70%; 95%; 100%; 100%; 100% EtOH) for 10 minutes each at room temperature. Samples were immersed in propylene oxide (Electron Microscopy Sciences) 3 x 10 minutes at room temperature, followed by a series of epon resin/propylene oxide (812 Epon Resin, Electron Microscopy Sciences) exchanges with increasing resin concentrations (50% resin/50% propylene oxide; 65% resin/35% propylene oxide; 75% resin/25% propylene oxide; 100% resin; 100% resin) for 90 minutes each. Tissues were transferred to BEEM capsules (Electron Microscopy Sciences) that were filled with 100% resin and polymerized for at least 48 hours at 60°C.

Transmission electron microscopy image acquisition

Plasticized sections were cut at 70 nm with a Histo Jumbo diamond knife (DiATOME) using a Leica UC7 ultramicrotome. Sections were decompressed using chloroform vapor and collected onto 3.05mm 200 mesh Gilder thin bar hexagonal mesh copper grids (T200H-Cu, Electron Microscopy Sciences). Sections were imaged unstained on a Hitachi HT7700 transmission electron microscope (HT7700, Hitachi High-Tech America, Inc.) at 80kV.

Eye injections

Intraocular eye injections were performed one day before tissue collection. Briefly, mice were anesthetized by inhalant isoflurane and sterile surgical spring scissors were used to gently part the eyelid to expose the corneoscleral junction. A small hole was made in the eye using a sterile 34-gauge needle and ~0.5 µL of cholera toxin subunit B conjugated with Alexa Fluor 488 (CTB-488, ThermoFisher Scientific, Catalogue Number: C34775) diluted in 0.9% sterile saline was intravitreally pressure-injected into the right eye using a pulled-glass micropipette coupled to a Picospritzer (Parker Hannifin).

dLGN tissue preparation for STORM imaging

Animals were deeply anesthetized with ketamine/xylazine and transcardially perfused with 5-10 mls of 37°C 0.9% sterile saline followed by 10 mls of room temperature 4% EM-Grade paraformaldehyde (PFA, Electron Microscopy Sciences) in 0.9% saline. Brains were embedded in 2.5% agarose and vibratome sectioned in the coronal plane at 100 µm. From the full anterior-posterior series of dLGN sections (~6-8 sections) we selected the central two sections for staining in all biological replicates. These sections

were morphologically consistent with Figs. 134-136 (5.07-5.31 mm) of the postnatal day 6 mouse brain from Paxinos's "Atlas of the developing mouse brain" Academic Press, 2020 [89]. Selected sections were postfixed in 4% PFA for 30 minutes at room temperature and washed for 30-40 minutes in 1X PBS. The dLGN was identified by the presence of CTB-488 signals using a fluorescence dissecting microscope. A circular tissue punch (~500 µm diameter) containing the dLGN was microdissected from each section using a blunt-end needle. A small microknife cut was made at the dorsal edge of the dLGN which, together with the CTB-488 signal, enabled us to identify the dLGN orientation during image acquisition.

Immunohistochemistry

We used a serial-section single-molecule localization imaging approach to prepare samples and collect super-resolution fluorescence imaging volumes as previously described [26]. dLGN tissue punches were blocked in 10% normal donkey serum (Jackson ImmunoResearch, Catalogue Number: 017-000-121) with 0.3% Triton X-100 (Sigma-Aldrich Inc.) and 0.02% sodium azide (Sigma-Aldrich Inc.) diluted in 1X PBS for 2-3 hours at room temperature and then incubated in primary antibodies for ~72 hours at 4°C. Primary antibodies used were Rabbit anti-Homer1 (Synaptic Systems, Catalogue Number: 160003, 1:100) to label postsynaptic densities (PSDs), mouse anti-Bassoon (Abcam, Catalogue Number AB82958, 1:100) to label presynaptic active zones (AZs), and guinea pig anti-VGluT2 (Millipore, Catalogue Number AB251-I, 1:100) to label presynaptic vesicles. Following primary antibody incubation, tissues were washed in 1X PBS for 6 x 20 minutes at room temperature and incubated in secondary

antibody solution overnight for ~36 hours at 4°C. The secondary antibodies used were donkey anti-rabbit IgG (Jackson ImmunoResearch, Catalogue Number 711-005-152, 1:100) conjugated with Dy749P1 (Dyomics, Catalogue Number 749P1-01) and Alexa Fluor 405 (ThermoFisher, Catalogue Number: A30000), donkey anti-mouse IgG (Jackson ImmunoResearch, Catalogue Number 715-005-150, 1:100) conjugated with Alexa Fluor 647 (ThermoFisher, Catalogue Number: A20006) and Alexa Fluor 405, and donkey anti-guinea pig IgG (Jackson ImmunoResearch, Catalogue Number 706-005-148, 1:100) conjugated with Cy3b (Cytiva, Catalogue Number: PA63101). Tissues were washed 6 x 20 minutes in 1X PBS at room temperature after secondary antibody incubation.

Postfixation, dehydration, and embedding in epoxy resin

Tissue embedding was performed as previously described [26]. Tissues were postfixed with 3% PFA + 0.1% GA (Electron Microscopy Sciences) in PBS for 2 hours at room temperature and then washed in 1X PBS for 20 minutes. To plasticize the tissues for ultrasectioning, the tissues were first dehydrated in a graded dilution series of 100% ethanol (50%/70%/90%/100%/100% EtOH) for 15 minutes each at room temperature and then immersed in a series of epoxy resin/100% EtOH exchanges (Electron Microscopy Sciences) with increasing resin concentration (25% resin/75% ethanol; 50% resin/50% ethanol; 75% resin/25% ethanol; 100% resin; 100% resin) for 2 hours each. Tissues were transferred to BEEM capsules (Electron Microscopy Sciences) that were filled with 100% resin and polymerized for 16 hours at 70°C.

Ultrasectioning

Plasticized tissue sections were cut using a Leica UC7 ultramicrotome at 70 nm using a Histo Jumbo diamond knife (DiATOME). Chloroform vapor was used to reduce compression after cutting. For each sample, ~100 sections were collected on a coverslip coated with 0.5% gelatin and 0.05% chromium potassium (Sigma-Aldrich Inc.), dried at 60 degrees for 25 minutes, and protected from light prior to imaging.

Imaging chamber preparation

Coverslips were chemically etched in 10% sodium ethoxide for 5 minutes at room temperature to remove the epoxy resin and expose the dyes to the imaging buffer for optimal photoswitching. Coverslips were then rinsed with ethanol and dH_2O. To create fiducial beads for flat-field and chromatic corrections, we mixed 715/755nm and 540/560nm, carboxylate-modified microspheres (Invitrogen, Catalogue Numbers F8799 and F8809, 1:8 ratio respectively) to create a high-density fiducial marker and then further diluted the mixture at 1:750 with Dulbecco's PBS to create a low-density bead solution. Both high- and low-density bead solutions were spotted on the coverslip (~0.7 µL each) for flat-field and chromatic aberration correction respectively. Excess beads were rinsed away with dH2O for 1-2 minutes. The coverslip was attached to a glass slide with double-sided tape to form an imaging chamber. The chamber was filled with STORM imaging buffer (10% glucose, 17.5µM glucose oxidase, 708nM catalase, 10mM MEA, 10mM NaCl, and 200mM Tris) and sealed with epoxy.

Imaging setup

Imaging was performed using a custom single-molecule super-resolution imaging system. The microscope contained low (4x/10x air) and high (60x 1.4NA oil immersion) magnitude objectives mounted on a commercial frame (Nikon Ti-U) with back optics arranged for oblique incident angle illumination. We used continuous-wave lasers at 488nm (Coherent), 561nm (MPB), 647nm (MPB), and 750nm (MPB) to excite Alexa 488, Cy3B, Alexa 647, and Dy749P1 dyes respectively. A 405 nm cube laser (Coherent) was used to reactivate Dy749P1 and Alexa647 dye photoswitching. The microscope was fitted with a custom pentaband/pentanotch dichroic filter set and a motorized emission filter wheel. The microscope also contained an IR laser-based focus lock system to maintain optimal focus during automatic image acquisition. Images were collected on 640*640-pixel region of an sCMOS camera (ORCA-Flash4.0 V3, Hamamatsu Photonics) with a pixel size of ~155 nm.

Automated image acquisition

Fiducials and tissue sections on the coverslip were imaged using the low magnification objective (4X) to create a mosaic overview of the specimen. Beads/sections were then imaged at high magnification (60X) to select regions of interest (ROIs) in the Cy3B and Alexa 488 channels. Before final image acquisition, laser intensities and the incident angle were adjusted to optimize photoswitching for STORM imaging and utilize the full dynamic range of the camera for conventional imaging.

Low-density bead images were taken in 16 partially overlapping ROIs. 715/755nm beads were excited using 750 nm light and images were collected through Dy749P1

and Alexa 647 emission filters. 540/560nm beads were excited using a 488 nm laser and images were collected through Alexa 647, Cy3B, and Alexa 488 emission filters. These fiducial images were later used to generate a non-linear warping transform to correct chromatic aberration. Next, ROIs within each tissue section were imaged at conventional (diffraction-limited) resolution in all four-color channels sequentially.

Following conventional image acquisition, a partially overlapping series of 9 images were collected in the high-density bead field for all 4 channels (Dy749P1, Alexa 647, Cy3B, and Alexa 488). These images were later used to perform a flat-field image correction of non-uniform laser illumination across the ROIs. Another round of bead images was taken as described above in a different ROI of the low-density bead field. These images were later used to confirm the stability of chromatic offsets during imaging. All ROIs within physical sections were then imaged by STORM for Dy749P1 and Alexa 647 channels. Images were acquired using a custom progression of increasing 405nm laser intensity to control single-molecule switching. 8000 frames of Dy749P1 channel images were collected (60 Hz imaging) followed by 12000 frames of Alexa 647 channel images (100 Hz). In a second imaging pass, the same ROIs were imaged for Cy3B and Alexa 488 channels, each for 8000 frames (60 Hz).

We imaged the ipsilateral and contralateral ROIs separately in each physical section of the dLGN. For consistency of ROI selection across biological replicates at each age, we identified the dorsal-ventral (DV) axis of the dLGN and selected ROIs within the center (core region) at 2/5 (ipsilateral ROI) and 4/5 (contralateral ROI) of the full DV length.

Image processing

Single-molecule localization was performed using a previously described DAOSTORM algorithm modified for use with sCMOS cameras [90, 91]. Molecule lists were rendered as 8-bit images with 15.5 nm pixel size where each molecule is plotted as an intensity distribution with an area reflecting its localization precision. Low-density fiducial images were used for chromatic aberration correction. We localized 715/755 beads in Dy749P1 and Alexa 647 channels, and 540/560 beads in Alexa 647, Cy3B, and Alexa 488 channels. A third-order polynomial transform map was generated by matching the positions of each bead in all channels to the Alexa 647 channel. The average residual error of bead matching was <15 nm for all channels. The transform maps were applied to both 4-color conventional and STORM images. Conventional images were upscaled (by 10X) to match the STORM image size. The method to align serial sections was previously described [26]. STORM images were first aligned to their corresponding conventional images by image correlation. To generate an aligned 3D image stack from serial sections, we normalized the intensity of all Alexa 488 images and used these normalized images to generate both rigid and elastic transformation matrices for all four-color channels of both STORM and conventional data. The final image stack was then rotated and cropped to exclude incompletely imaged edge areas. To further confirm that the processed region corresponds to the contralateral dLGN, conventional CTB(+) signals of the labeled contralateral projection were thresholded to create a polygonal mask (a convex hull analysis linking the outermost CTB signals in the image volume).

The mask was then applied to STORM images to exclude peripheral areas where CTB signals were absent or faint.

Cell body filter

The aligned STORM images had non-specific labeling of cell bodies in Dy749P1 and Alexa 647 channels corresponding to Homer1 and Bassoon immunolabels. To limit synaptic cluster identification to the neuropil region we identified cell bodies based on their Dy749P1 signal and excluded these regions from further image processing. STORM images were convolved with a Gaussian function (σ=140 nm) and then binarized using the lower threshold of a two-level Otsu threshold method. We located connected components in the thresholded images and generated a mask based on components larger than e^{11} voxels. Because cell body clusters were orders of magnitude larger than synaptic clusters, the cell body filter algorithm was robust to a range of size thresholds. The mask was applied to images of all channels to exclude cell body areas.

Eye-specific synapse identification and quantification

To correct for minor variance in image intensity across physical sections, we normalized the pixel intensity histogram of each section to the average histogram of all sections. Image histograms were rescaled to make full use of the 8-bit range. Using a two-level Otsu threshold method, the conventional images were thresholded into three classes: a low-intensity background, low-intensity signals above the background representing non-synaptic labeling, and high-intensity signals representing synaptic structures. The

conventional images were binarized by the lower two-level Otsu threshold, generating a mask for STORM images to filter out background signals. STORM images were convolved with a Gaussian function (σ= 77.5 nm) and thresholded using the higher two-level Otsu threshold. Following thresholding, connected components were identified in three dimensions using MATLAB 'conncomp' function. A watershedding approach was applied to split large clusters that were improperly connected. Clusters were kept for further analysis only if they contained aligned image information across two or more physical sections. We also removed all edge synapses from our analysis by excluding synapses that did not have blank image data on all adjacent sides.

To distinguish non-specific immunolabeling from true synaptic signals, we quantified two parameters for each cluster: cluster volume and cluster signal density calculated by the ratio of within-cluster pixels with positive signal intensity in the raw STORM images. Two separate populations were identified in 2D histograms plotted from these two parameters. We manually selected the population with higher volumes and signal densities representing synaptic structures. To test the robustness of the manual selection, we performed multiple repeated measurements of the same data and discovered a between-measurement variance of <1% (data not shown).

To identify paired pre- and postsynaptic clusters, we first measured the centroid-centroid distance of each cluster in the Dy749P1 (Homer1) and Alexa 647 (Bassoon) channels to the closest cluster in the other channel. We next quantified the signal intensity of each opposing synaptic channel within a 140 nm shell surrounding each

cluster. A 2D histogram was plotted based on the measured centroid-centroid distances and opposing channel signal densities of each cluster. Paired clusters with closely positioned centroids and high intensities of apposed channel signal were identified using the OPTICS algorithm. Retinogeniculate synapses were identified by pairing Bassoon (Alexa 647) clusters with VGluT2 (Cy3B) clusters using the same method as pre/post-synaptic pairing. Synapses from the right eye were identified by pairing VGluT2 clusters with CTB (Alexa 488) clusters. The volume of each cluster reflected the total voxel volume of all connected voxels, and the total signal intensity was a sum of voxel intensity within the volume of the connected voxels.

Multi-AZ synapse identification and quantification

To determine whether an eye-specific VGluT2 cluster is a mAZ synapse or a sAZ synapse, we measured the number of active zones (defined by individual Bassoon clusters) associated with each VGluT2 cluster in the dataset. A 3D shell was extended 140 nm from the surface voxels of each VGluT2 cluster and any Bassoon clusters that fell within the shell were considered to be associated with the target VGluT2 cluster. The number of active zones (AZs) associated with each VGluT2 cluster was then measured. VGluT2 clusters associated with more than 1 AZ were defined as mAZ synapses, while those associated with only 1 AZ were defined as sAZ synapses.

Quantification of mAZ and sAZ synapse VGluT2 cluster volume was performed using the "regionprops" function in MATLAB, which provided the voxel size and weighted centroid of each VGluT2 cluster. The search for sAZ synapses adjacent to mAZ

synapses (synaptic clustering analysis) was conducted using a similar search approach as for associated Bassoon clusters, with expansion shell sizes ranging from 1 μm to 4 μm from the surface voxels of each mAZ synapse. The main Figs. in the study utilized an expansion distance of 1.5 μm. An eye-specific sAZ synapse was considered to be near a mAZ synapse if its weighted centroid fell within the expanded volume.

Quantification and statistical analysis

Statistical analysis was performed using SPSS. Plots were generated by SPSS or R (ggplot2). Statistical details are presented in the figure legends and supplemental tables S2/S3. For all measurements in this paper, we analyzed N = 3 biological replicates (individual mice) for each genotype (WT and β2KO) at each age (P2, P4, and P8). Cluster densities, synapse AZ number, average VGluT2 cluster volume, and all fractional measurements were presented as mean ± SEM values in paired bar graphs and statistical analysis was performed using two-tailed paired T-tests. Nonparametric Kolmogorov-Smirnov tests were used in all cumulative histogram comparisons. We used a linear mixed model to compare VGluT2 cluster volumes (Figs. 3 and S2) and distance measurements (Figs. 5 and S5). For VGluT2 cluster volume comparisons, the age or eye-of-origin was the fixed main factor and biological replicate IDs were nested random factors. In distance measurement comparisons, the mAZ synapse AZ number was the fixed main factor and biological replicate IDs were nested random factors. Effect sizes were calculated using Cohen's d for parametric tests and epsilon squared for nonparametric tests. To address multiple testing, we applied false discovery rate (FDR) correction using the Benjamini-Hochberg method with $\alpha = 0.05$ separately within

each experimental condition (P2-WT, P2-ß2KO, P4-WT, P4-ß2KO, P8-WT, P8-ß2KO). 20-34 measurements (varying by age and genotype) were corrected within each of the six experimental conditions, resulting in condition-specific FDR-adjusted p-values presented in Table S2. In violin plots, each violin showed the distribution of grouped data from all biological replicates from the same condition. Each black dot represents the median value of each biological replicate, and the horizontal black line represents the group median. Black lines connect measurements of CTB(+) and CTB(-) populations from the same biological replicate. Asterisks in all figures indicate statistical significance after FDR correction: *p(adj)<0.05. For VGluT2 volume comparisons, we calculated 5/95% confidence intervals based on the linear mixed model. 5/95% confidence intervals in synapse densities, AZ numbers, and distances were calculated for paired or unpaired data comparisons using SPSS. All statistical results are listed in Table S2. All conclusions we draw in the main text from the data have corresponding confidence intervals listed in both the figure legends and Table S3.

Acknowledgements:

We thank Drs. Michael C. Crair (Yale University) and Eric M. Ullian (University of California, San Francisco) for generously sharing the β2KO and ET33^{Cre} mouse lines used in this work. We are grateful to Tim Maugel in the Laboratory for Biological Ultrastructure (UMD) for his assistance with transmission electron microscopy experiments. The research was funded by National Institutes of Health grant DP2MH125812 (C.M.S.).

Author contributions:

Conceptualization, C.Z. and C.M.S.; data curation, C.Z., T.V., C.M.S.; formal analysis, C.Z. and C.M.S.; funding acquisition, C.M.S.; investigation, C.Z., T.V., C.M.S.; methodology, C.Z., T.V., C.M.S.; project administration, C.Z. and C.M.S.; resources, C.Z., T.V., C.M.S.; software, C.Z. and C.M.S.; supervision, C.M.S.; validation, C.Z., T.V., C.M.S.; visualization, C.Z., T.V., C.M.S.; writing – original draft preparation, C.Z. and C.M.S.; writing – review & editing, C.Z., T.V., C.M.S.

Figure legends:

Fig. 1: Retinogeniculate boutons form multiple active zones during eye-specific competition

(A) Experimental design. CTB-Alexa 488 was injected into the right eye of wild-type and β2KO mice. One day after the treatment, tissue was collected from the left dLGN at P2, P4, and P8. Red squares indicate the STORM imaging regions that were analyzed. (B) Representative examples of individual sAZ and mAZ inputs, with corresponding active zone counts ranging from one to three. Upper panels show Z-projections of inputs and lower panels show the corresponding 3D volume. Arrowheads point to individual Bassoon clusters (active zones) paired with postsynaptic Homer1 labels within each input. All examples are from a WT P8 sample. (C) Electron micrographs of mAZ retinogeniculate inputs in a P8 ET33^{Cre}::ROSA26$^{LSL\text{-}Matrix\text{-}dAPEX2}$ mouse. Darkly-stained dAPEX2(+) mitochondria are present within ipsilaterally-projecting RGC

terminals. Arrowheads point to electron-dense material at the postsynaptic density, apposed to individual active zones with clustered presynaptic synaptic vesicles.

Fig. 2: Changes in eye-specific input density during synaptic competition

(A) Representative Z-projection images of mAZ and sAZ inputs across ages and genotypes. Arrowheads point to individual Bassoon/Homer1 cluster pairs indicating release sites. (B) Representative CTB(+) dominant-eye (top panels) and CTB(-) non-dominant-eye (bottom panels) mAZ inputs in a WT P8 sample, showing synaptic (left panels), CTB (middle panels), and merged labels (right panels). Arrowheads point to individual Bassoon/Homer1 paired clusters. (C) Eye-specific mAZ (left) and sAZ (right) input density across development in WT (top panels) and β2KO mice (bottom panels). Black dots represent mean values from separate biological replicates and black lines connect eye-specific measurements within each replicate (N=3 for each age and genotype). Error bars represent group means ± SEMs. Statistical significance between eye-specific measurements was assessed for each genotype using two-tailed paired T-tests with Benjamini-Hochberg FDR correction ($\alpha = 0.05$) at each age. *p(adj)<0.05.

Fig. 3: Dominant-eye inputs show larger vesicle pools that scale with active zone number

(A and B) Violin plots showing the distribution of VGluT2 cluster volume for (A) mAZ and (B) sAZ inputs in WT (filled) and β2KO mice (striped) at each age. The width of each violin plot reflects the relative synapse proportions across the entire grouped data set at each age (N=3 biological replicates) and the maximum width was normalized across all

groups. The black dots represent the median value of each biological replicate (N=3), and the black horizontal lines represent the median value of all inputs grouped across replicates. Black lines connect measurements of CTB(+) and CTB(-) populations from the same biological replicate. Statistical significance was determined using a linear mixed model ANOVA with a post-hoc Bonferroni correction, followed by Benjamini-Hochberg FDR correction ($\alpha = 0.05$) for multiple comparisons at each age/genotype. Black asterisks indicate significant eye-specific differences at each age. *p(adj)<0.05. (C) Eye-specific VGluT2 signal volume for all inputs separated by number of AZs in WT (left panel) and β2KO mice (right panel) at P4. (D) Average VGluT2 volume per AZ for all inputs separated by number of AZs in WT (left panel) and β2KO mice (right panel) at P4. In panels (C) and (D), error bars indicate group means ± SEMs (N=3 biological replicates for each age and genotype). Black dots represent mean values from separate biological replicates and black lines connect eye-specific measurements within each replicate. Statistical significance between eye-specific measurements was assessed for each genotype using two-tailed paired T-tests with Benjamini-Hochberg FDR correction ($\alpha = 0.05$): *p(adj)<0.05.

Fig. 4: Eye-specific synapse clustering before eye-opening

(A) Representative mAZ (left panels) and sAZ (right panels) inputs in a WT P8 sample with nearby sAZ synapses (arrowheads) clustered within 1.5 μm (dashed yellow ring). Arrows point to the centered mAZ or sAZ inputs. (B) Ratio of clustered and isolated mAZ and sAZ inputs for CTB(+) (upper panels) and CTB(-) (lower panels) inputs in WT and β2KO mice at P4. (C) Comparison of the clustered input ratio between mAZ and

sAZ inputs across different ages, genotypes, and eyes of origin. (D) Comparison of the average number of nearby sAZ synapses for clustered mAZ and sAZ inputs across different ages, genotypes, and eyes of origin. In panels B-D, black dots represent mean values from separate biological replicates and black lines connect measurements within each replicate (N=3 for each age and genotype). Error bars represent group means ± SEMs. For each genotype, two-tailed paired T-tests with Benjamini-Hochberg FDR correction (α = 0.05) were used to test statistical significance between mAZ and sAZ inputs at each age. *p(adj)<0.05.

Fig. 5: Clustered mAZ inputs are closer than isolated inputs during competition

(A-B) Distance between clustered and isolated mAZ inputs and the closest like-eye clustered mAZ input, shown for (A) CTB(+) and (B) CTB(-) projections at P4 in WT and β2KO mice. Boxes indicate the 25%-75% distribution of input measurements from N=3 biological replicates and whiskers extend to 1.5 times the interquartile range. Gray dots represent individual distance measurements for all mAZ inputs. Black and red dots represent mean values from separate biological replicates and black lines connect measurements within each replicate (N=3 for each age and genotype). Statistical significance was determined using a linear mixed model ANOVA with post-hoc Bonferroni correction. For each genotype, p-values were corrected for multiple testing with Benjamini-Hochberg FDR correction (α = 0.05) at each age. Black asterisks indicate significant differences. *p(adj)<0.05.

Fig. S1: Fraction of mAZ inputs across development, related to Fig. 2

Eye-specific mAZ input fraction across development in WT (top panel) and β2KO mice (bottom panel). Black dots represent mean values from separate biological replicates and black lines connect measurements within each replicate (N=3 for each age and genotype). Error bars represent group means ± SEMs. Statistical significance between eye-specific measurements was assessed for each genotype using two-tailed paired T-tests with Benjamini-Hochberg FDR correction (α = 0.05) at each age. *p(adj)<0.05.

Fig. S2: Quantification of docked vesicle pool volume and AZ number in mAZ and sAZ inputs, related to Fig. 2.

(A-C) Violin plots show the distribution of VGluT2 cluster volume within a 70 nm shell surround individual Bassoon clusters at (A) P2, (B) P4, and (C) P8. The width of each violin plot reflects the relative synapse proportions at each volume across the entire grouped data set (N=3 biological replicates). The maximum width of the violin plots was normalized across all groups. Black horizontal lines represent the median value of all inputs grouped across replicates. The black dots represent the median value of each biological replicate and black lines between dots connect measurements from the same biological replicate. Statistical significance was determined using a linear mixed model ANOVA with post-hoc Bonferroni correction. See Table S3 for 5/95% confidence intervals. (D-E) Average AZ number per mAZ input in (D) WT and (E) β2KO mice. Black dots represent mean values from separate biological replicates (N = 3) and black lines connect measurements within each replicate. Error bars represent means ± SEMs. Statistical significance was assessed for each genotype using two-tailed paired T-tests with Benjamini-Hochberg FDR correction (α = 0.05) at each age. *p(adj)<0.05.

Fig. S3: Relationship between vesicle pool volume and active zone number, related to Fig. 3.

(A) Total VGluT2 volume per input and (B) average VGluT2 volume per AZ for all inputs separated by number of AZs in WT (filled bars) and β2KO mice (striped bars) at P2. (C) Total VGluT2 volume per input and (D) average VGluT2 volume per AZ for all inputs separated by number of AZs in WT (filled bars) and β2KO mice (striped bars) at P8. In all panels, error bars indicate group means ± SEMs (N=3 biological replicates for each age and genotype). Black dots represent mean values from separate biological replicates and black lines connect measurements within each replicate. Statistical significance between eye-specific measurements was assessed for each genotype using two-tailed paired T-tests with Benjamini-Hochberg FDR correction ($\alpha = 0.05$) at each age: *p(adj)<0.05.

Fig. S4: sAZ synapse clustering near like-eye mAZ inputs, related to Fig. 4

(A) The ratio of CTB(+) dominant-eye and (B) CTB(-) non-dominant-eye sAZ synapses nearby like-eye mAZ inputs within increasing distance cutoffs in WT samples across ages. At distances of 1-2 µm across all ages, the observed ratios (filled bars) are higher than a reshuffling of the data (open bars) where the position of sAZ inputs was randomized within the neuropil. (C-D) Percentage of sAZ synapses within 1.5 µm of opposite-eye mAZ inputs across ages in WT and β2KO mice. Data are compared against a randomization of sAZ positions (open bars) as in panels A/B. For all panels, error bars represent group means ± SEMs (N=3 biological replicates for each age and

genotype). Black dots represent mean values from separate biological replicates and black lines connect measurements within each replicate. Statistical significance was assessed for each genotype using two-tailed paired T-tests with Benjamini-Hochberg FDR correction (α = 0.05) at each age: *p(adj)<0.05.

Fig. S5: Clustered and isolated mAZ inputs show similar spacing after competition, related to Fig. 5.

(A-B) Distance between clustered and isolated mAZ inputs and the closest like-eye clustered mAZ input, shown for (A) CTB(+) and (B) CTB(-) projections at P8 in WT and β2KO mice. Boxes indicate the 25%-75% distribution of input measurements from N=3 biological replicates and whiskers extend to 1.5 times the interquartile range. Gray dots represent individual distance measurements for all mAZ inputs. Black and red dots represent mean values from separate biological replicates and black lines connect measurements within each replicate (N=3 for each age and genotype). Statistical significance was determined using a linear mixed model ANOVA with post-hoc Bonferroni correction (see Table S3 for 5/95% confidence intervals). For each genotype, p-values were corrected for multiple testing with Benjamini-Hochberg FDR correction (α = 0.05) at each age.

Fig. S6: sAZ synapse vesicle pool volume is independent of distance to mAZ inputs, related to Fig. 5.

(A) Cumulative distributions of VGluT2 volume for CTB(+) dominant-eye or (B) CTB(-) non-dominant-eye sAZ synapses near (<1.5 μm) or far from (>1.5 μm) like-eye mAZ

inputs. The distributions show merged data across all ages (P2/P4/P8; N=3 biological replicates at each time point). A nonparametric Kolmogorov-Smirnov test was used for statistical analysis (see Table S3 for 5/95% confidence intervals). For each genotype, p-values were corrected for multiple testing with Benjamini-Hochberg FDR correction (α = 0.05) at each age.

References:

1. Rall W. Electrophysiology of a dendritic neuron model. Biophys J. 1962;2(2 Pt 2):145-67. doi: 10.1016/s0006-3495(62)86953-7. PubMed PMID: 14490040; PMCID: PMC1366481.
2. Mel B, editor. The Clusteron: Toward a Simple Abstraction for a Complex Neuron1991 1991: Morgan-Kaufmann.
3. Poirazi P, Mel BW. Impact of active dendrites and structural plasticity on the memory capacity of neural tissue. Neuron. 2001;29(3):779-96. doi: 10.1016/s0896-6273(01)00252-5. PubMed PMID: 11301036.
4. Mel BW, Schiller J, Poirazi P. Synaptic plasticity in dendrites: complications and coping strategies. Curr Opin Neurobiol. 2017;43:177-86. Epub 20170425. doi: 10.1016/j.conb.2017.03.012. PubMed PMID: 28453975.
5. Kastellakis G, Poirazi P. Synaptic Clustering and Memory Formation. Front Mol Neurosci. 2019;12:300. Epub 20191206. doi: 10.3389/fnmol.2019.00300. PubMed PMID: 31866824; PMCID: PMC6908852.
6. Winnubst J, Lohmann C. Synaptic clustering during development and learning: the why, when, and how. Front Mol Neurosci. 2012;5:70. Epub 20120531. doi: 10.3389/fnmol.2012.00070. PubMed PMID: 22666187; PMCID: PMC3364493.
7. Leighton AH, Lohmann C. The Wiring of Developing Sensory Circuits-From Patterned Spontaneous Activity to Synaptic Plasticity Mechanisms. Front Neural Circuits. 2016;10:71. Epub 20160905. doi: 10.3389/fncir.2016.00071. PubMed PMID: 27656131; PMCID: PMC5011135.
8. Kirchner JH, Gjorgjieva J. Emergence of synaptic organization and computation in dendrites2022;28(1):21-30. doi: doi:10.1515/nf-2021-0031.
9. Liang L, Chen C. Organization, Function, and Development of the Mouse Retinogeniculate Synapse. Annu Rev Vis Sci. 2020;6:261-85. doi: 10.1146/annurev-vision-121219-081753. PubMed PMID: 32936733.
10. Bickford ME, Slusarczyk A, Dilger EK, Krahe TE, Kucuk C, Guido W. Synaptic development of the mouse dorsal lateral geniculate nucleus. J Comp Neurol. 2010;518(5):622-35. doi: 10.1002/cne.22223. PubMed PMID: 20034053; PMCID: PMC4278806.

915 11. Monavarfeshani A, Stanton G, Van Name J, Su K, Mills WA, 3rd, Swilling K, Kerr A,
916 Huebschman NA, Su J, Fox MA. LRRTM1 underlies synaptic convergence in visual thalamus. Elife.
917 2018;7. Epub 20180209. doi: 10.7554/eLife.33498. PubMed PMID: 29424692; PMCID:
918 PMC5826289.
919 12. Hong YK, Park S, Litvina EY, Morales J, Sanes JR, Chen C. Refinement of the
920 retinogeniculate synapse by bouton clustering. Neuron. 2014;84(2):332-9. Epub 20141002. doi:
921 10.1016/j.neuron.2014.08.059. PubMed PMID: 25284005; PMCID: PMC4322918.
922 13. Mason CA. Development of terminal arbors of retino-geniculate axons in the kitten--I.
923 Light microscopical observations. Neuroscience. 1982;7(3):541-59. doi: 10.1016/0306-
924 4522(82)90063-x. PubMed PMID: 7070666.
925 14. Hamos JE, Van Horn SC, Raczkowski D, Sherman SM. Synaptic circuits involving an
926 individual retinogeniculate axon in the cat. J Comp Neurol. 1987;259(2):165-92. doi:
927 10.1002/cne.902590202. PubMed PMID: 3584556.
928 15. Hammer S, Monavarfeshani A, Lemon T, Su J, Fox MA. Multiple Retinal Axons Converge
929 onto Relay Cells in the Adult Mouse Thalamus. Cell Rep. 2015;12(10):1575-83. Epub 20150828.
930 doi: 10.1016/j.celrep.2015.08.003. PubMed PMID: 26321636; PMCID: PMC5757867.
931 16. Morgan JL, Berger DR, Wetzel AW, Lichtman JW. The Fuzzy Logic of Network
932 Connectivity in Mouse Visual Thalamus. Cell. 2016;165(1):192-206. doi:
933 10.1016/j.cell.2016.02.033. PubMed PMID: 27015312; PMCID: PMC4808248.
934 17. Budisantoso T, Matsui K, Kamasawa N, Fukazawa Y, Shigemoto R. Mechanisms
935 Underlying Signal Filtering at a Multisynapse Contact. J Neurosci. 2012;32(7):2357. doi:
936 10.1523/JNEUROSCI.5243-11.2012.
937 18. Sherman SM, Guillery RW. On the actions that one nerve cell can have on another:
938 distinguishing "drivers" from "modulators". Proc Natl Acad Sci U S A. 1998;95(12):7121-6. doi:
939 10.1073/pnas.95.12.7121. PubMed PMID: 9618549; PMCID: PMC22761.
940 19. Guillery RW, Sherman SM. Thalamic Relay Functions and Their Role in Corticocortical
941 Communication: Generalizations from the Visual System. Neuron. 2002;33(2):163-75. doi:
942 10.1016/S0896-6273(01)00582-7.
943 20. Sretavan D, Shatz CJ. Prenatal development of individual retinogeniculate axons during
944 the period of segregation. Nature. 1984;308(5962):845-8. doi: 10.1038/308845a0. PubMed
945 PMID: 6201743.
946 21. Sretavan DW, Shatz CJ. Prenatal development of retinal ganglion cell axons: segregation
947 into eye-specific layers within the cat's lateral geniculate nucleus. J Neurosci. 1986;6(1):234-51.
948 doi: 10.1523/JNEUROSCI.06-01-00234.1986. PubMed PMID: 3944621; PMCID: PMC6568631.
949 22. Dhande OS, Hua EW, Guh E, Yeh J, Bhatt S, Zhang Y, Ruthazer ES, Feller MB, Crair MC.
950 Development of single retinofugal axon arbors in normal and beta2 knock-out mice. J Neurosci.
951 2011;31(9):3384-99. doi: 10.1523/JNEUROSCI.4899-10.2011. PubMed PMID: 21368050; PMCID:
952 PMC3060716.
953 23. Campbell G, Shatz CJ. Synapses formed by identified retinogeniculate axons during the
954 segregation of eye input. J Neurosci. 1992;12(5):1847-58. doi: 10.1523/JNEUROSCI.12-05-
955 01847.1992. PubMed PMID: 1578274; PMCID: PMC6575897.
956 24. Chen C, Regehr WG. Developmental remodeling of the retinogeniculate synapse.
957 Neuron. 2000;28(3):955-66. doi: 10.1016/s0896-6273(00)00166-5. PubMed PMID: 11163279.

958 25. Hauser JL, Liu X, Litvina EY, Chen C. Prolonged synaptic currents increase relay neuron
959 firing at the developing retinogeniculate synapse. J Neurophysiol. 2014;112(7):1714-28. Epub
960 20140625. doi: 10.1152/jn.00451.2014. PubMed PMID: 24966302; PMCID: PMC4157180.
961 26. Zhang C, Yadav S, Speer CM. The synaptic basis of activity-dependent eye-specific
962 competition. Cell Rep. 2023;42(2):112085. Epub 20230207. doi: 10.1016/j.celrep.2023.112085.
963 PubMed PMID: 36753422.
964 27. Vatan T, Minehart JA, Zhang C, Agarwal V, Yang J, Speer CM. Volumetric super-
965 resolution imaging by serial ultrasectioning and stochastic optical reconstruction microscopy in
966 mouse neural tissue. STAR Protocols. 2021;2(4):100971. doi: 10.1016/j.xpro.2021.100971.
967 28. Muir-Robinson G, Hwang BJ, Feller MB. Retinogeniculate axons undergo eye-specific
968 segregation in the absence of eye-specific layers. J Neurosci. 2002;22(13):5259-64. doi:
969 10.1523/jneurosci.22-13-05259.2002. PubMed PMID: 12097474; PMCID: PMC6758243.
970 29. Xu HP, Burbridge TJ, Chen MG, Ge X, Zhang Y, Zhou ZJ, Crair MC. Spatial pattern of
971 spontaneous retinal waves instructs retinotopic map refinement more than activity frequency.
972 Dev Neurobiol. 2015;75(6):621-40. Epub 20150330. doi: 10.1002/dneu.22288. PubMed PMID:
973 25787992; PMCID: PMC4697738.
974 30. Xu HP, Furman M, Mineur YS, Chen H, King SL, Zenisek D, Zhou ZJ, Butts DA, Tian N,
975 Picciotto MR, Crair MC. An instructive role for patterned spontaneous retinal activity in mouse
976 visual map development. Neuron. 2011;70(6):1115-27. doi: 10.1016/j.neuron.2011.04.028.
977 PubMed PMID: 21689598; PMCID: PMC3119851.
978 31. Xu HP, Burbridge TJ, Ye M, Chen M, Ge X, Zhou ZJ, Crair MC. Retinal Wave Patterns Are
979 Governed by Mutual Excitation among Starburst Amacrine Cells and Drive the Refinement and
980 Maintenance of Visual Circuits. J Neurosci. 2016;36(13):3871-86. doi:
981 10.1523/JNEUROSCI.3549-15.2016. PubMed PMID: 27030771; PMCID: PMC4812142.
982 32. Rossi FM, Pizzorusso T, Porciatti V, Marubio LM, Maffei L, Changeux JP. Requirement of
983 the nicotinic acetylcholine receptor beta 2 subunit for the anatomical and functional
984 development of the visual system. Proc Natl Acad Sci U S A. 2001;98(11):6453-8. Epub
985 20010508. doi: 10.1073/pnas.101120998. PubMed PMID: 11344259; PMCID: PMC33489.
986 33. Grubb MS, Rossi FM, Changeux JP, Thompson ID. Abnormal functional organization in
987 the dorsal lateral geniculate nucleus of mice lacking the beta 2 subunit of the nicotinic
988 acetylcholine receptor. Neuron. 2003;40(6):1161-72. doi: 10.1016/s0896-6273(03)00789-x.
989 PubMed PMID: 14687550.
990 34. Sun C, Warland DK, Ballesteros JM, van der List D, Chalupa LM. Retinal waves in mice
991 lacking the beta2 subunit of the nicotinic acetylcholine receptor. Proc Natl Acad Sci U S A.
992 2008;105(36):13638-43. Epub 20080829. doi: 10.1073/pnas.0807178105. PubMed PMID:
993 18757739; PMCID: PMC2527347.
994 35. Stafford BK, Sher A, Litke AM, Feldheim DA. Spatial-temporal patterns of retinal waves
995 underlying activity-dependent refinement of retinofugal projections. Neuron. 2009;64(2):200-
996 12. doi: 10.1016/j.neuron.2009.09.021. PubMed PMID: 19874788; PMCID: PMC2771121.
997 36. Bansal A, Singer JH, Hwang BJ, Xu W, Beaudet A, Feller MB. Mice lacking specific
998 nicotinic acetylcholine receptor subunits exhibit dramatically altered spontaneous activity
999 patterns and reveal a limited role for retinal waves in forming ON and OFF circuits in the inner
1000 retina. J Neurosci. 2000;20(20):7672-81. doi: 10.1523/jneurosci.20-20-07672.2000. PubMed
1001 PMID: 11027228; PMCID: PMC6772851.

1002 37. Hammer S, Carrillo GL, Govindaiah G, Monavarfeshani A, Bircher JS, Su J, Guido W, Fox
1003 MA. Nuclei-specific differences in nerve terminal distribution, morphology, and development in
1004 mouse visual thalamus. Neural Dev. 2014;9:16. Epub 20140710. doi: 10.1186/1749-8104-9-16.
1005 PubMed PMID: 25011644; PMCID: PMC4108237.
1006 38. Zhang Q, Lee WA, Paul DL, Ginty DD. Multiplexed peroxidase-based electron microscopy
1007 labeling enables simultaneous visualization of multiple cell types. Nat Neurosci. 2019;22(5):828-
1008 39. Epub 20190318. doi: 10.1038/s41593-019-0358-7. PubMed PMID: 30886406; PMCID:
1009 PMC6555422.
1010 39. Koch SM, Dela Cruz CG, Hnasko TS, Edwards RH, Huberman AD, Ullian EM. Pathway-
1011 specific genetic attenuation of glutamate release alters select features of competition-based
1012 visual circuit refinement. Neuron. 2011;71(2):235-42. doi: 10.1016/j.neuron.2011.05.045.
1013 PubMed PMID: 21791283; PMCID: PMC3375067.
1014 40. Su J, Byer L, Liang Y, Fox MA. Distribution, development, and identity of retinal ganglion
1015 cells labeled in the Sert-Cre reporter mouse. Journal of Comparative Neurology.
1016 2024;532(3):e25606. doi: https://doi.org/10.1002/cne.25606.
1017 41. Johnson KP, Fitzpatrick MJ, Zhao L, Wang B, McCracken S, Williams PR, Kerschensteiner
1018 D. Cell-type-specific binocular vision guides predation in mice. Neuron. 2021;109(9):1527-39.e4.
1019 Epub 20210329. doi: 10.1016/j.neuron.2021.03.010. PubMed PMID: 33784498; PMCID:
1020 PMC8112612.
1021 42. Assali A, Gaspar P, Rebsam A. Activity dependent mechanisms of visual map formation--
1022 from retinal waves to molecular regulators. Semin Cell Dev Biol. 2014;35:136-46. Epub
1023 20140822. doi: 10.1016/j.semcdb.2014.08.008. PubMed PMID: 25152335.
1024 43. Fassier C, Nicol X. Retinal Axon Interplay for Binocular Mapping. Front Neural Circuits.
1025 2021;15:679440. Epub 20210604. doi: 10.3389/fncir.2021.679440. PubMed PMID: 34149367;
1026 PMCID: PMC8213063.
1027 44. Penn AA, Riquelme PA, Feller MB, Shatz CJ. Competition in retinogeniculate patterning
1028 driven by spontaneous activity. Science. 1998;279(5359):2108-12. doi:
1029 10.1126/science.279.5359.2108. PubMed PMID: 9516112.
1030 45. Assali A, Le Magueresse C, Bennis M, Nicol X, Gaspar P, Rebsam A. RIM1/2 in retinal
1031 ganglion cells are required for the refinement of ipsilateral axons and eye-specific segregation.
1032 Sci Rep. 2017;7(1):3236. Epub 20170612. doi: 10.1038/s41598-017-03361-0. PubMed PMID:
1033 28607399; PMCID: PMC5468276.
1034 46. Fredj NB, Hammond S, Otsuna H, Chien C-B, Burrone J, Meyer MP. Synaptic Activity and
1035 Activity-Dependent Competition Regulates Axon Arbor Maturation, Growth Arrest, and
1036 Territory in the Retinotectal Projection. J Neurosci. 2010;30(32):10939. doi:
1037 10.1523/JNEUROSCI.1556-10.2010.
1038 47. Hua JY, Smear MC, Baier H, Smith SJ. Regulation of axon growth in vivo by activity-based
1039 competition. Nature. 2005;434(7036):1022-6. doi: 10.1038/nature03409. PubMed PMID:
1040 15846347.
1041 48. Rahman TN, Munz M, Kutsarova E, Bilash OM, Ruthazer ES. Stentian structural plasticity
1042 in the developing visual system. Proc Natl Acad Sci U S A. 2020;117(20):10636-8. Epub
1043 20200504. doi: 10.1073/pnas.2001107117. PubMed PMID: 32366647; PMCID: PMC7245132.

1044 49. Munz M, Gobert D, Schohl A, Poquérusse J, Podgorski K, Spratt P, Ruthazer ES. Rapid
1045 Hebbian axonal remodeling mediated by visual stimulation. Science. 2014;344(6186):904-9. doi:
1046 10.1126/science.1251593. PubMed PMID: 24855269.
1047 50. Zhang LI, Tao HW, Holt CE, Harris WA, Poo M-m. A critical window for cooperation and
1048 competition among developing retinotectal synapses. Nature. 1998;395(6697):37-44. doi:
1049 10.1038/25665.
1050 51. Matsumoto N, Barson D, Liang L, Crair MC. Hebbian instruction of axonal connectivity by
1051 endogenous correlated spontaneous activity. Science. 2024;385(6710):eadh7814. Epub
1052 20240816. doi: 10.1126/science.adh7814. PubMed PMID: 39146415.
1053 52. Yasuda M, Nagappan-Chettiar S, Johnson-Venkatesh EM, Umemori H. An activity-
1054 dependent determinant of synapse elimination in the mammalian brain. Neuron.
1055 2021;109(8):1333-49 e6. Epub 20210325. doi: 10.1016/j.neuron.2021.03.006. PubMed PMID:
1056 33770504; PMCID: PMC8068677.
1057 53. Louail A, Sierksma MC, Chaffiol A, Baudet S, Assali A, Couvet S, Nedjam M, Roche F,
1058 Zagar Y, Duebel J, Nicol X. cAMP-Dependent Co-stabilization of Axonal Arbors from Adjacent
1059 Developing Neurons. Cell Rep. 2020;33(1):108220. doi: 10.1016/j.celrep.2020.108220. PubMed
1060 PMID: 33027659.
1061 54. Kutsarova E, Schohl A, Munz M, Wang A, Zhang YY, Bilash OM, Ruthazer ES. BDNF
1062 signaling in correlation-dependent structural plasticity in the developing visual system. PLoS
1063 Biol. 2023;21(4):e3002070. Epub 20230403. doi: 10.1371/journal.pbio.3002070. PubMed PMID:
1064 37011100; PMCID: PMC10101647.
1065 55. Godement P, Salaün J, Imbert M. Prenatal and postnatal development of
1066 retinogeniculate and retinocollicular projections in the mouse. J Comp Neurol.
1067 1984;230(4):552-75. doi: 10.1002/cne.902300406. PubMed PMID: 6520251.
1068 56. Mooney R, Madison DV, Shatz CJ. Enhancement of transmission at the developing
1069 retinogeniculate synapse. Neuron. 1993;10(5):815-25. doi: 10.1016/0896-6273(93)90198-z.
1070 PubMed PMID: 8388224.
1071 57. Ziburkus J, Dilger EK, Lo FS, Guido W. LTD and LTP at the developing retinogeniculate
1072 synapse. J Neurophysiol. 2009;102(6):3082-90. Epub 20090923. doi: 10.1152/jn.90618.2008.
1073 PubMed PMID: 19776360; PMCID: PMC2804430.
1074 58. Butts DA, Kanold PO, Shatz CJ. A burst-based "Hebbian" learning rule at retinogeniculate
1075 synapses links retinal waves to activity-dependent refinement. PLoS Biol. 2007;5(3):e61. doi:
1076 10.1371/journal.pbio.0050061. PubMed PMID: 17341130; PMCID: PMC1808114.
1077 59. Lee H, Brott BK, Kirkby LA, Adelson JD, Cheng S, Feller MB, Datwani A, Shatz CJ. Synapse
1078 elimination and learning rules co-regulated by MHC class I H2-Db. Nature. 2014;509(7499):195-
1079 200. Epub 20140330. doi: 10.1038/nature13154. PubMed PMID: 24695230; PMCID:
1080 PMC4016165.
1081 60. Chung WS, Clarke LE, Wang GX, Stafford BK, Sher A, Chakraborty C, Joung J, Foo LC,
1082 Thompson A, Chen C, Smith SJ, Barres BA. Astrocytes mediate synapse elimination through
1083 MEGF10 and MERTK pathways. Nature. 2013;504(7480):394-400. Epub 20131124. doi:
1084 10.1038/nature12776. PubMed PMID: 24270812; PMCID: PMC3969024.
1085 61. Stevens B, Allen NJ, Vazquez LE, Howell GR, Christopherson KS, Nouri N, Micheva KD,
1086 Mehalow AK, Huberman AD, Stafford B, Sher A, Litke AM, Lambris JD, Smith SJ, John SW, Barres

1087 BA. The classical complement cascade mediates CNS synapse elimination. Cell.
1088 2007;131(6):1164-78. doi: 10.1016/j.cell.2007.10.036. PubMed PMID: 18083105.
1089 62. Schafer DP, Lehrman EK, Kautzman AG, Koyama R, Mardinly AR, Yamasaki R, Ransohoff
1090 RM, Greenberg ME, Barres BA, Stevens B. Microglia sculpt postnatal neural circuits in an activity
1091 and complement-dependent manner. Neuron. 2012;74(4):691-705. doi:
1092 10.1016/j.neuron.2012.03.026. PubMed PMID: 22632727; PMCID: PMC3528177.
1093 63. Hooks BM, Chen C. Distinct roles for spontaneous and visual activity in remodeling of
1094 the retinogeniculate synapse. Neuron. 2006;52(2):281-91. doi: 10.1016/j.neuron.2006.07.007.
1095 PubMed PMID: 17046691.
1096 64. Dilger EK, Krahe TE, Morhardt DR, Seabrook TA, Shin HS, Guido W. Absence of plateau
1097 potentials in dLGN cells leads to a breakdown in retinogeniculate refinement. J Neurosci.
1098 2015;35(8):3652-62. doi: 10.1523/jneurosci.2343-14.2015. PubMed PMID: 25716863; PMCID:
1099 PMC4339365.
1100 65. Cork RJ, Namkung Y, Shin HS, Mize RR. Development of the visual pathway is disrupted
1101 in mice with a targeted disruption of the calcium channel beta(3)-subunit gene. J Comp Neurol.
1102 2001;440(2):177-91. doi: 10.1002/cne.1378. PubMed PMID: 11745616.
1103 66. Fernández-Nogales M, López-Cascales MT, Murcia-Belmonte V, Escalante A, Fernández-
1104 Albert J, Muñoz-Viana R, Barco A, Herrera E. Multiomic Analysis of Neurons with Divergent
1105 Projection Patterns Identifies Novel Regulators of Axon Pathfinding. Adv Sci (Weinh).
1106 2022;9(29):e2200615. Epub 20220821. doi: 10.1002/advs.202200615. PubMed PMID:
1107 35988153; PMCID: PMC9561852.
1108 67. Wang Q, Marcucci F, Cerullo I, Mason C. Ipsilateral and Contralateral Retinal Ganglion
1109 Cells Express Distinct Genes during Decussation at the Optic Chiasm. eneuro.
1110 2016;3(6):ENEURO.0169-16.2016. doi: 10.1523/ENEURO.0169-16.2016.
1111 68. Nicol X, Voyatzis S, Muzerelle A, Narboux-Nême N, Südhof TC, Miles R, Gaspar P. cAMP
1112 oscillations and retinal activity are permissive for ephrin signaling during the establishment of
1113 the retinotopic map. Nat Neurosci. 2007;10(3):340-7. Epub 20070128. doi: 10.1038/nn1842.
1114 PubMed PMID: 17259982.
1115 69. Balice-Gordon RJ, Chua CK, Nelson CC, Lichtman JW. Gradual loss of synaptic cartels
1116 precedes axon withdrawal at developing neuromuscular junctions. Neuron. 1993;11(5):801-15.
1117 doi: 10.1016/0896-6273(93)90110-d. PubMed PMID: 8240805.
1118 70. Gan WB, Lichtman JW. Synaptic segregation at the developing neuromuscular junction.
1119 Science. 1998;282(5393):1508-11. doi: 10.1126/science.282.5393.1508. PubMed PMID:
1120 9822385.
1121 71. Wyatt RM, Balice-Gordon RJ. Activity-dependent elimination of neuromuscular synapses.
1122 J Neurocytol. 2003;32(5-8):777-94. doi: 10.1023/b:Neur.0000020623.62043.33. PubMed PMID:
1123 15034267.
1124 72. Chen J, Mizushige T, Nishimune H. Active zone density is conserved during synaptic
1125 growth but impaired in aged mice. J Comp Neurol. 2012;520(2):434-52. doi: 10.1002/cne.22764.
1126 PubMed PMID: 21935939; PMCID: PMC3731066.
1127 73. Balice-Gordon RJ, Lichtman JW. Long-term synapse loss induced by focal blockade of
1128 postsynaptic receptors. Nature. 1994;372(6506):519-24. doi: 10.1038/372519a0. PubMed PMID:
1129 7990923.

1130 74. Buffelli M, Burgess RW, Feng G, Lobe CG, Lichtman JW, Sanes JR. Genetic evidence that
1131 relative synaptic efficacy biases the outcome of synaptic competition. Nature.
1132 2003;424(6947):430-4. doi: 10.1038/nature01844. PubMed PMID: 12879071.
1133 75. Kopp DM, Perkel DJ, Balice-Gordon RJ. Disparity in neurotransmitter release probability
1134 among competing inputs during neuromuscular synapse elimination. J Neurosci.
1135 2000;20(23):8771-9. doi: 10.1523/jneurosci.20-23-08771.2000. PubMed PMID: 11102485;
1136 PMCID: PMC6773052.
1137 76. Sanes JR, Lichtman JW. Development of the vertebrate neuromuscular junction. Annu
1138 Rev Neurosci. 1999;22:389-442. doi: 10.1146/annurev.neuro.22.1.389. PubMed PMID:
1139 10202544.
1140 77. Misgeld T, Kummer TT, Lichtman JW, Sanes JR. Agrin promotes synaptic differentiation
1141 by counteracting an inhibitory effect of neurotransmitter. Proc Natl Acad Sci USA.
1142 2005;102(31):11088-93. doi: 10.1073/pnas.0504806102.
1143 78. Lin W, Dominguez B, Yang J, Aryal P, Brandon EP, Gage FH, Lee KF. Neurotransmitter
1144 acetylcholine negatively regulates neuromuscular synapse formation by a Cdk5-dependent
1145 mechanism. Neuron. 2005;46(4):569-79. doi: 10.1016/j.neuron.2005.04.002. PubMed PMID:
1146 15944126.
1147 79. Hashimoto K, Kano M. Synapse elimination in the developing cerebellum. Cell Mol Life
1148 Sci. 2013;70(24):4667-80. Epub 20130628. doi: 10.1007/s00018-013-1405-2. PubMed PMID:
1149 23811844; PMCID: PMC3830199.
1150 80. Bosman LW, Konnerth A. Activity-dependent plasticity of developing climbing fiber-
1151 Purkinje cell synapses. Neuroscience. 2009;162(3):612-23. Epub 20090123. doi:
1152 10.1016/j.neuroscience.2009.01.032. PubMed PMID: 19302832.
1153 81. Hashimoto K, Kano M. Functional differentiation of multiple climbing fiber inputs during
1154 synapse elimination in the developing cerebellum. Neuron. 2003;38(5):785-96. doi:
1155 10.1016/s0896-6273(03)00298-8. PubMed PMID: 12797962.
1156 82. Nitta A, Yamasaki M, Miyazaki T, Konno K, Yoshimura H, Watanabe M. Molecular and
1157 Anatomical Strengthening of "Winner" Climbing Fiber Synapses in Developing Mouse Purkinje
1158 Cells. J Neurosci. 2025. Epub 20250227. doi: 10.1523/JNEUROSCI.2156-24.2025. PubMed PMID:
1159 40015986.
1160 83. Wilson AM, Schalek R, Suissa-Peleg A, Jones TR, Knowles-Barley S, Pfister H, Lichtman
1161 JW. Developmental Rewiring between Cerebellar Climbing Fibers and Purkinje Cells Begins with
1162 Positive Feedback Synapse Addition. Cell Rep. 2019;29(9):2849-61.e6. doi:
1163 https://doi.org/10.1016/j.celrep.2019.10.081.
1164 84. Bosman LWJ, Takechi H, Hartmann J, Eilers J, Konnerth A. Homosynaptic Long-Term
1165 Synaptic Potentiation of the “Winner” Climbing Fiber Synapse in Developing Purkinje Cells. J
1166 Neurosci. 2008;28(4):798. doi: 10.1523/JNEUROSCI.4074-07.2008.
1167 85. Ohtsuki G, Hirano T. Bidirectional plasticity at developing climbing fiber-Purkinje neuron
1168 synapses. Eur J Neurosci. 2008;28(12):2393-400. Epub 20081121. doi: 10.1111/j.1460-
1169 9568.2008.06539.x. PubMed PMID: 19032589.
1170 86. Lorenzetto E, Caselli L, Feng G, Yuan W, Nerbonne JM, Sanes JR, Buffelli M. Genetic
1171 perturbation of postsynaptic activity regulates synapse elimination in developing cerebellum.
1172 Proc Natl Acad Sci USA. 2009;106(38):16475-80. doi: 10.1073/pnas.0907298106.

1173 87. Kawamura Y, Nakayama H, Hashimoto K, Sakimura K, Kitamura K, Kano M. Spike timing-
1174 dependent selective strengthening of single climbing fibre inputs to Purkinje cells during
1175 cerebellar development. Nat Commun. 2013;4(1):2732. doi: 10.1038/ncomms3732.
1176 88. Benninger K, Hood G, Simmel D, Tuite L, Wetzel A, Ropelewski A, Watkins S, Watson A,
1177 Bruchez M. Cyberinfrastructure of a Multi-Petabyte Microscopy Resource for Neuroscience
1178 Research. Practice and Experience in Advanced Research Computing; Portland, OR, USA:
1179 Association for Computing Machinery; 2020. p. 1–7.
1180 89. Paxinos G. Atlas of the developing mouse brain at E17.5, P0 and P6. 1st ed. Amsterdam ;
1181 Boston: Elsevier; 2007. xi, 353 p. p.
1182 90. Babcock H, Sigal YM, Zhuang X. A high-density 3D localization algorithm for stochastic
1183 optical reconstruction microscopy. Optical Nanoscopy. 2012;1(6). doi: 10.1186/2192-2853-1-6.
1184 91. Babcock HP, Huang F, Speer CM. Correcting Artifacts in Single Molecule Localization
1185 Microscopy Analysis Arising from Pixel Quantum Efficiency Differences in sCMOS Cameras. Sci
1186 Rep. 2019;9(1):18058. Epub 20191202. doi: 10.1038/s41598-019-53698-x. PubMed PMID:
1187 31792238; PMCID: PMC6889274.
1188

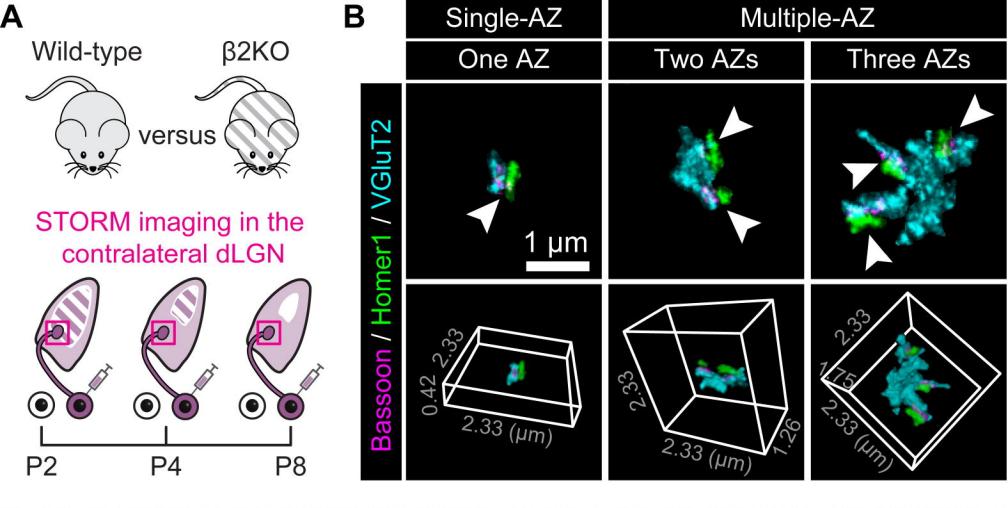
A
Wild-type
β2KO
versus
STORM imaging in the contralateral dLGN
P2
P4
P8
B
Single-AZ
Multiple-AZ
One AZ
Two AZs
Three AZs
Bassoon / Homer1 / VGluT2
1 µm
0.42
2.33
2.33 (µm)
2.33
1.26
2.33 (µm)
2.33
1.75
2.33 (µm)

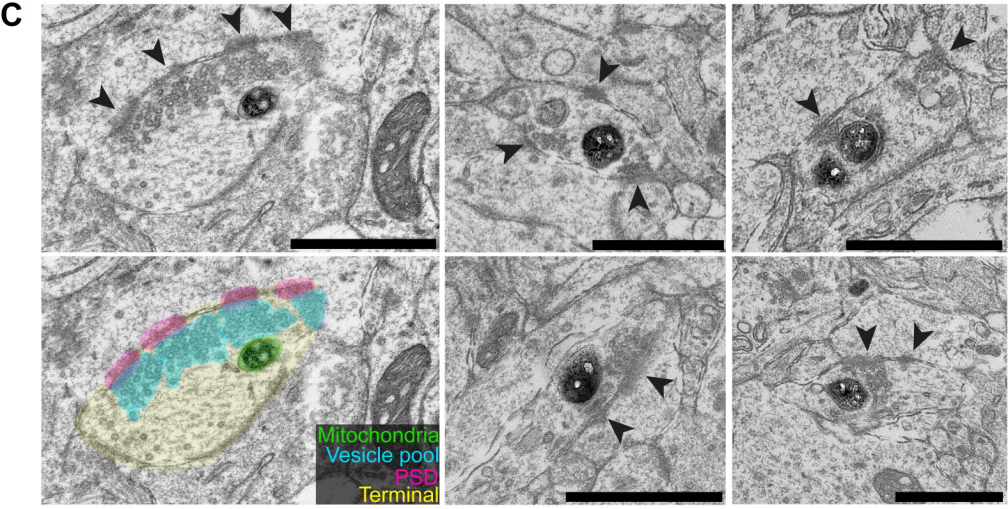
C
Mitochondria
Vesicle pool
PSD
Terminal

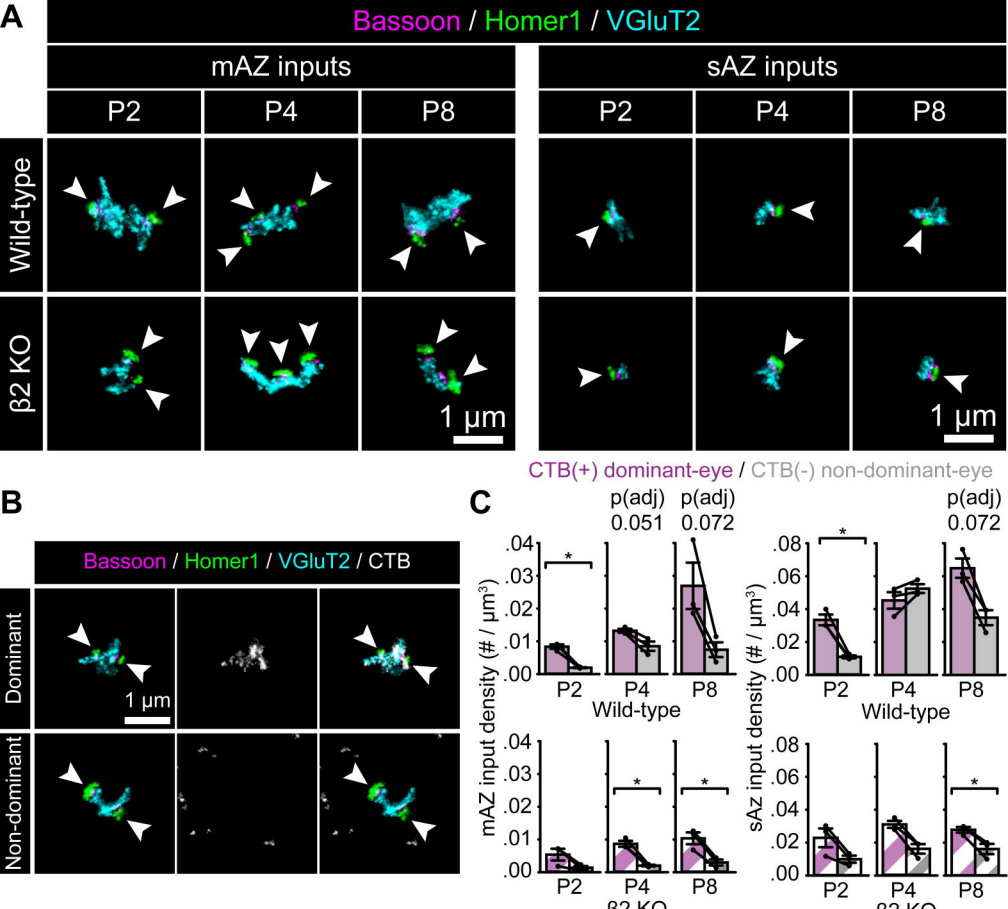
A
Bassoon / Homer1 / VGluT2
mAZ inputs
sAZ inputs
P2
P4
P8
Wild-type
β2 KO
1 µm
B
Bassoon / Homer1 / VGluT2 / CTB
Dominant
Non-dominant
CTB(+) dominant-eye / CTB(-) non-dominant-eye
C
p(adj)
0.051
0.072
mAZ input density (# / µm³)
sAz input density (# / µm³)
Wild-type
β2 KO

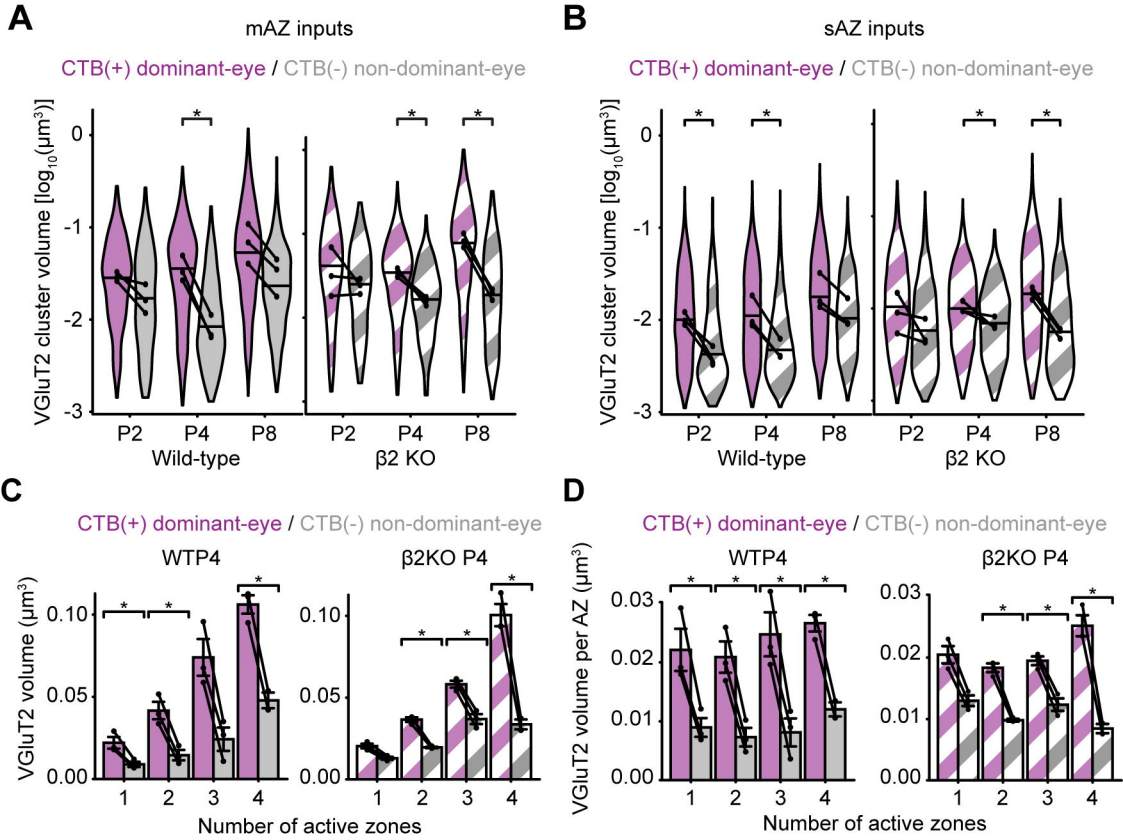
A
mAZ inputs
CTB(+) dominant-eye / CTB(-) non-dominant-eye
VGluT2 cluster volume [log10(μm3)]
0
-1
-2
-3
*
P2
P4
P8
Wild-type
β2 KO
B
sAZ inputs
CTB(+) dominant-eye / CTB(-) non-dominant-eye
VGluT2 cluster volume [log10(μm3)]
C
CTB(+) dominant-eye / CTB(-) non-dominant-eye
WTP4
β2KO P4
VGluT2 volume (μm3)
0.10
0.05
0.00
1
2
3
4
Number of active zones
D
CTB(+) dominant-eye / CTB(-) non-dominant-eye
WTP4
β2KO P4
VGluT2 volume per AZ (μm3)
0.03
0.02
0.01
0.00
Number of active zones

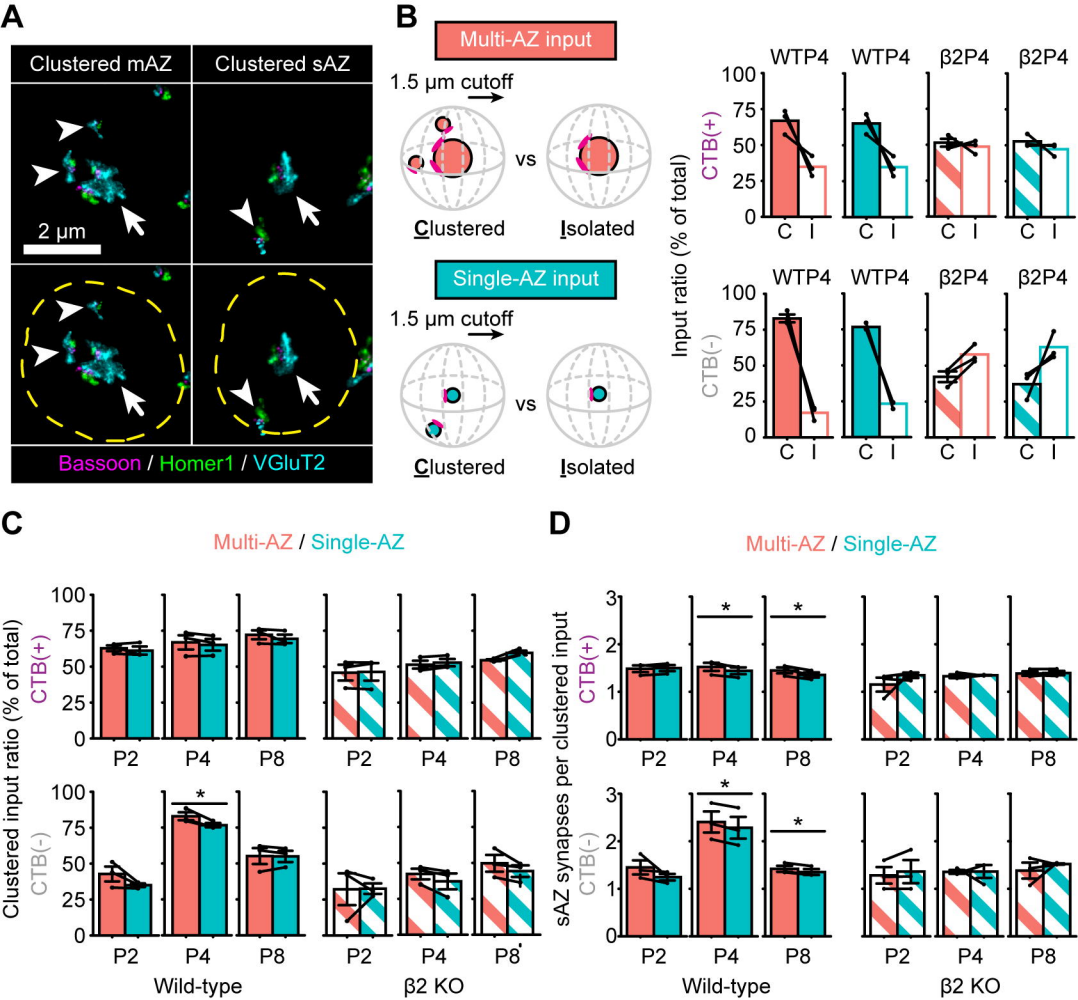
A
Clustered mAZ
Clustered sAZ
2 µm
Bassoon / Homer1 / VGluT2
B
Multi-AZ input
1.5 µm cutoff
vs
Clustered
Isolated
Single-AZ input
1.5 µm cutoff
vs
Clustered
Isolated
WTP4
WTP4
β2P4
β2P4
CTB(+)
CTB(-)
Input ratio (% of total)
C
I
C
Multi-AZ / Single-AZ
Clustered input ratio (% of total)
CTB(+)
CTB(-)
P2
P4
P8
Wild-type
β2 KO
D
Multi-AZ / Single-AZ
sAZ synapses per clustered input
CTB(+)
CTB(-)
Wild-type
β2 KO

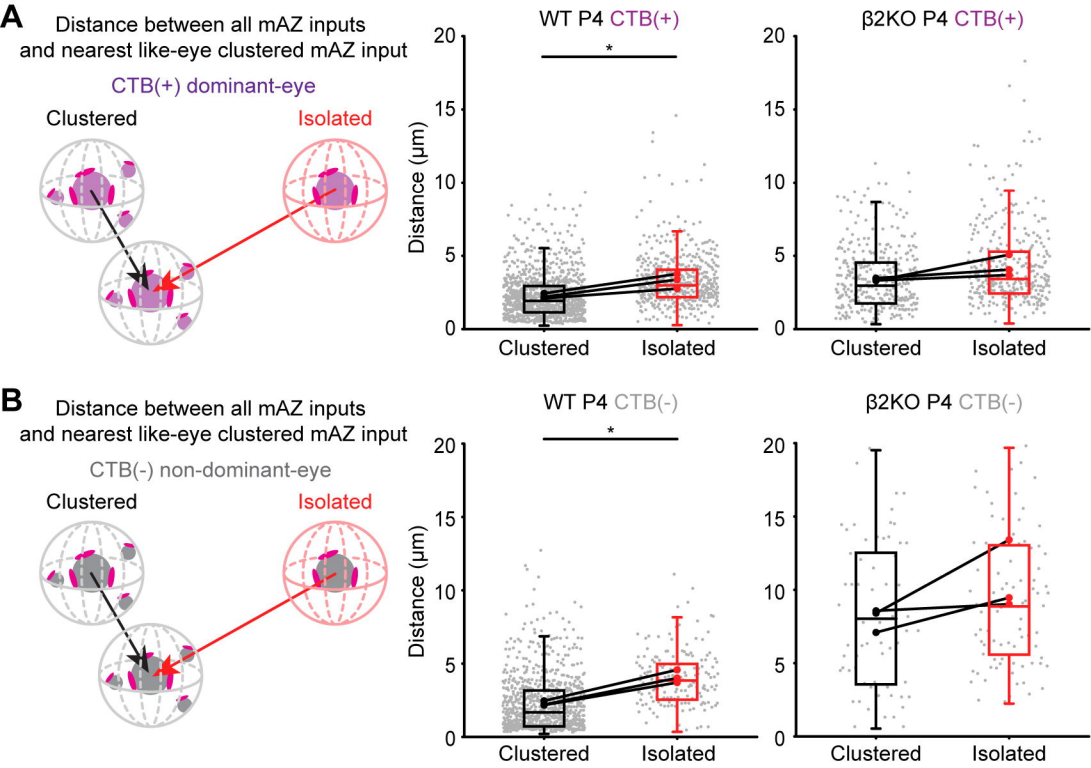
A
Distance between all mAZ inputs
and nearest like-eye clustered mAZ input
CTB(+) dominant-eye
Clustered
Isolated
WT P4 CTB(+)
β2KO P4 CTB(+)
Distance (µm)
*
Clustered
Isolated
B
Distance between all mAZ inputs
and nearest like-eye clustered mAZ input
CTB(-) non-dominant-eye
Clustered
Isolated
WT P4 CTB(-)
β2KO P4 CTB(-)
Distance (µm)
*
Clustered
Isolated

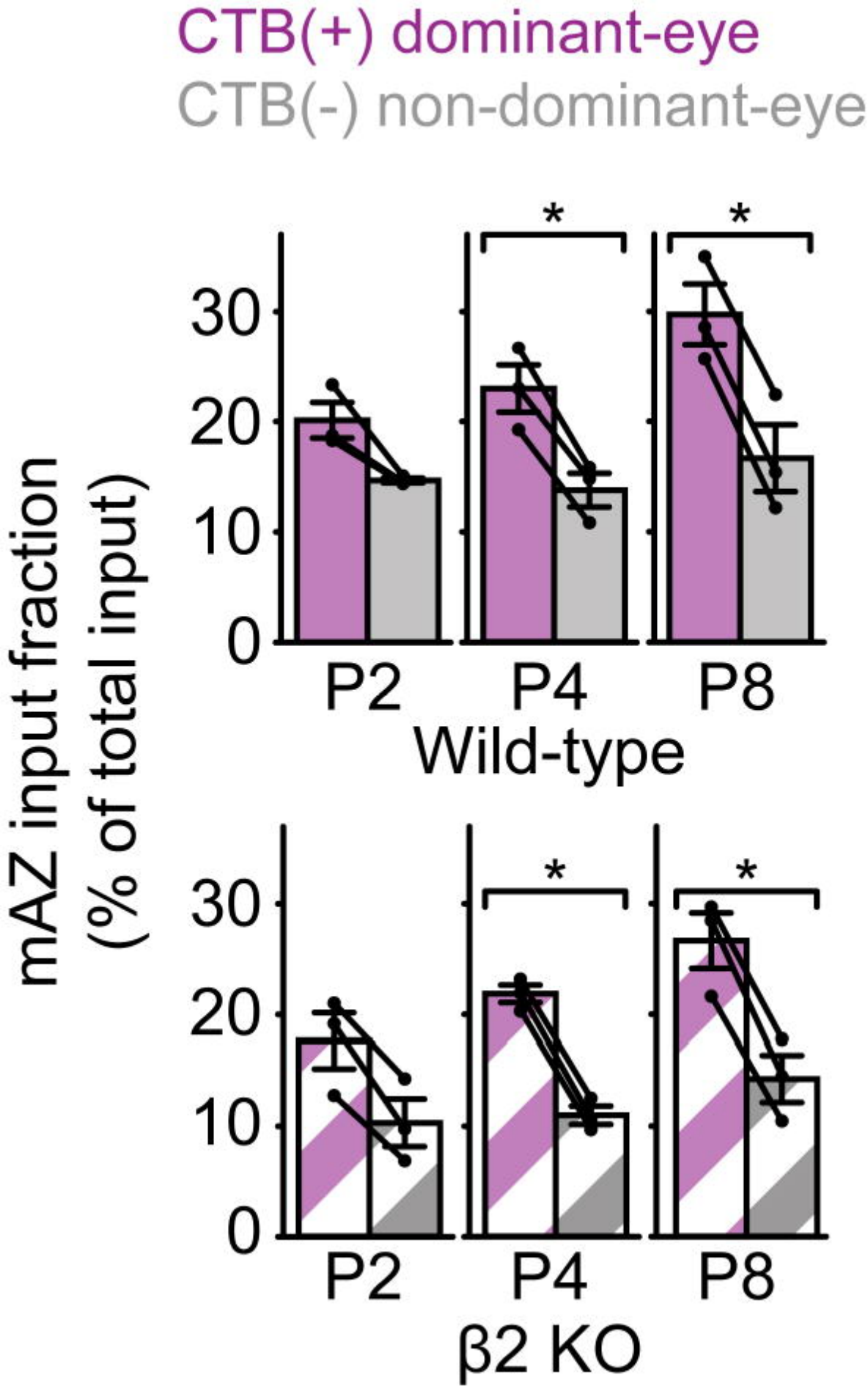
CTB(+) dominant-eye
CTB(-) non-dominant-eye
mAZ input fraction
(% of total input)
30
20
10
0
*
*
P2
P4
P8
Wild-type
30
20
10
0
*
*
P2
P4
P8
β2 KO

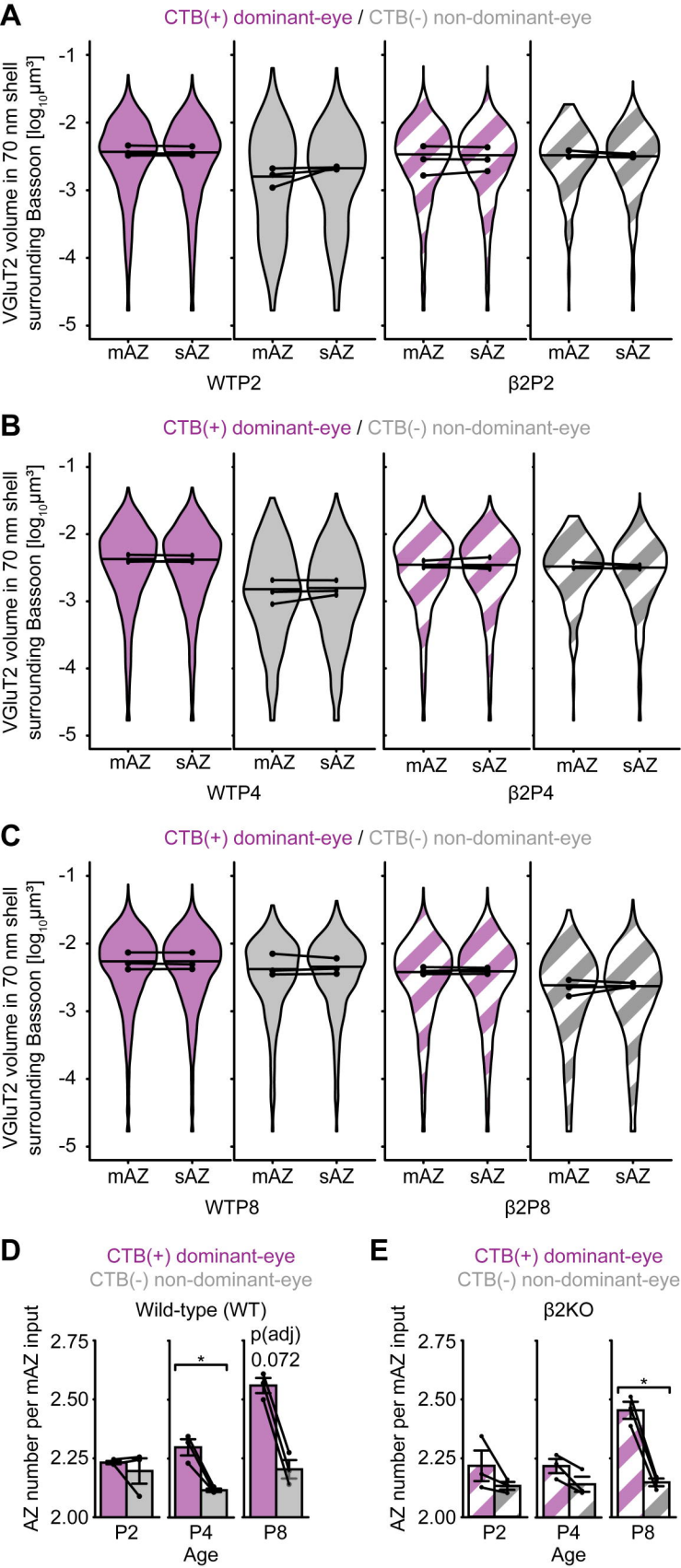
A
CTB(+) dominant-eye / CTB(-) non-dominant-eye
VGluT2 volume in 70 nm shell surrounding Bassoon [log10µm³]
-1
-2
-3
-4
-5
mAZ
sAZ
WTP2
β2P2
B
CTB(+) dominant-eye / CTB(-) non-dominant-eye
WTP4
β2P4
C
CTB(+) dominant-eye / CTB(-) non-dominant-eye
WTP8
β2P8
D
CTB(+) dominant-eye
CTB(-) non-dominant-eye
Wild-type (WT)
AZ number per mAZ input
2.75
2.50
2.25
2.00
*
p(adj)
0.072
P2
P4
P8
Age
E
CTB(+) dominant-eye
CTB(-) non-dominant-eye
β2KO
AZ number per mAZ input
2.75
2.50
2.25
2.00
*
P2
P4
P8
Age

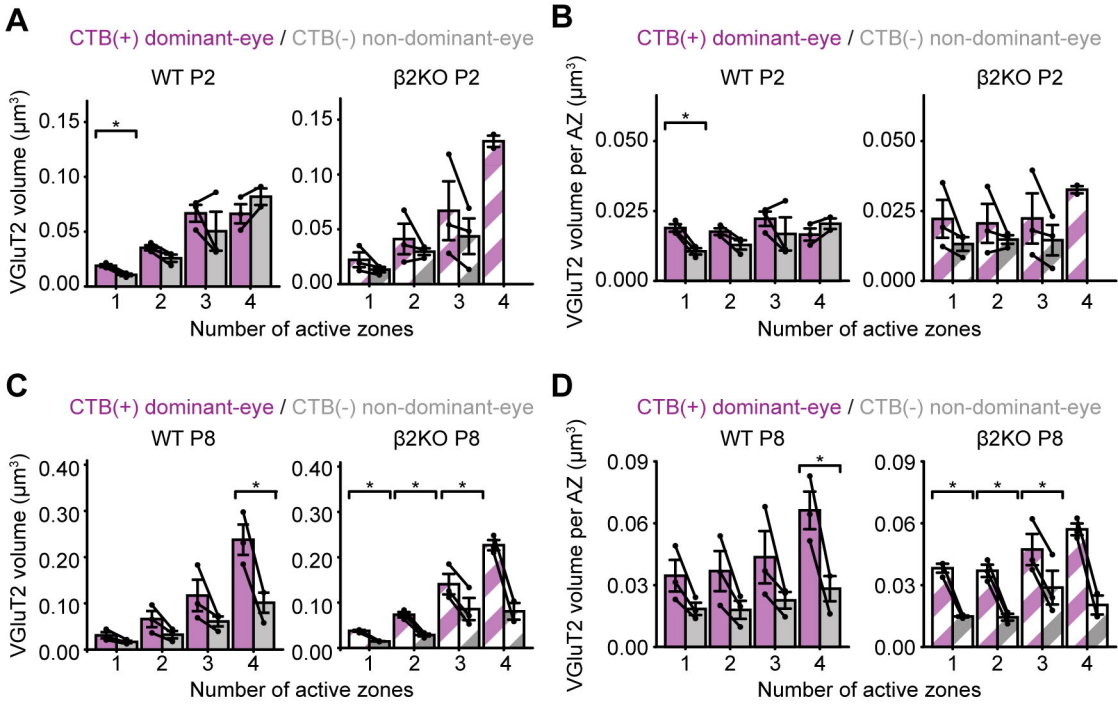
A
CTB(+) dominant-eye / CTB(-) non-dominant-eye
WT P2
β2KO P2
VGluT2 volume (μm³)
0.15
0.10
0.05
0.00
*
1
2
3
4
Number of active zones
B
CTB(+) dominant-eye / CTB(-) non-dominant-eye
WT P2
β2KO P2
VGluT2 volume per AZ (μm³)
0.050
0.025
0.000
*
1
2
3
4
Number of active zones
C
CTB(+) dominant-eye / CTB(-) non-dominant-eye
WT P8
β2KO P8
VGluT2 volume (μm³)
0.40
0.30
0.20
0.10
0.00
*
1
2
3
4
Number of active zones
D
CTB(+) dominant-eye / CTB(-) non-dominant-eye
WT P8
β2KO P8
VGluT2 volume per AZ (μm³)
0.09
0.06
0.03
0.00
*
1
2
3
4
Number of active zones

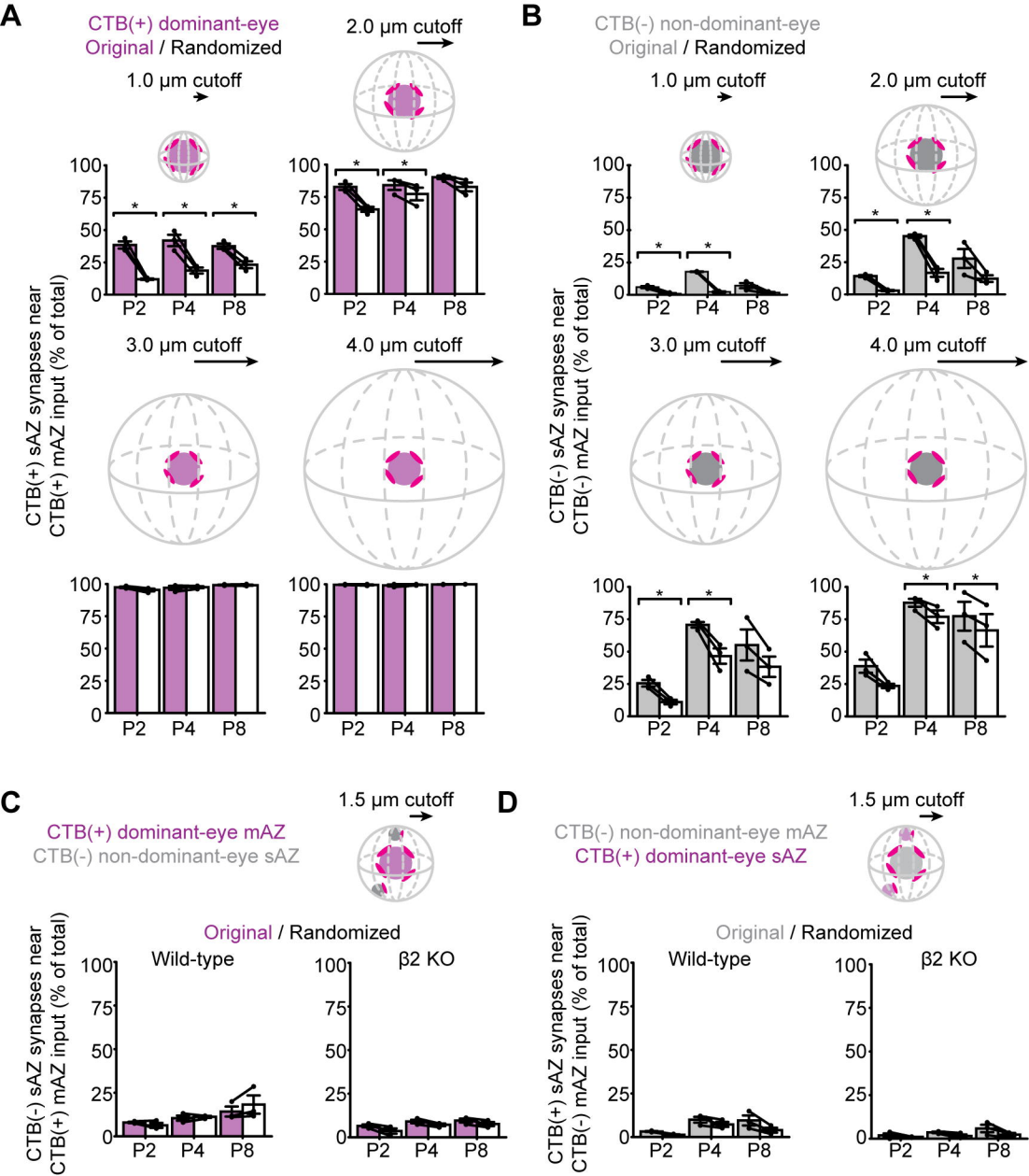
A
CTB(+) dominant-eye
Original / Randomized
1.0 µm cutoff
2.0 µm cutoff
3.0 µm cutoff
4.0 µm cutoff
CTB(+) sAZ synapses near
CTB(+) mAZ input (% of total)
B
CTB(-) non-dominant-eye
Original / Randomized
CTB(-) sAZ synapses near
CTB(-) mAZ input (% of total)
C
1.5 µm cutoff
CTB(+) dominant-eye mAZ
CTB(-) non-dominant-eye sAZ
Original / Randomized
Wild-type
β2 KO
CTB(-) sAZ synapses near
CTB(+) mAZ input (% of total)
D
1.5 µm cutoff
CTB(-) non-dominant-eye mAZ
CTB(+) dominant-eye sAZ
Original / Randomized
Wild-type
β2 KO
CTB(+) sAZ synapses near
CTB(-) mAZ input (% of total)
P2
P4
P8

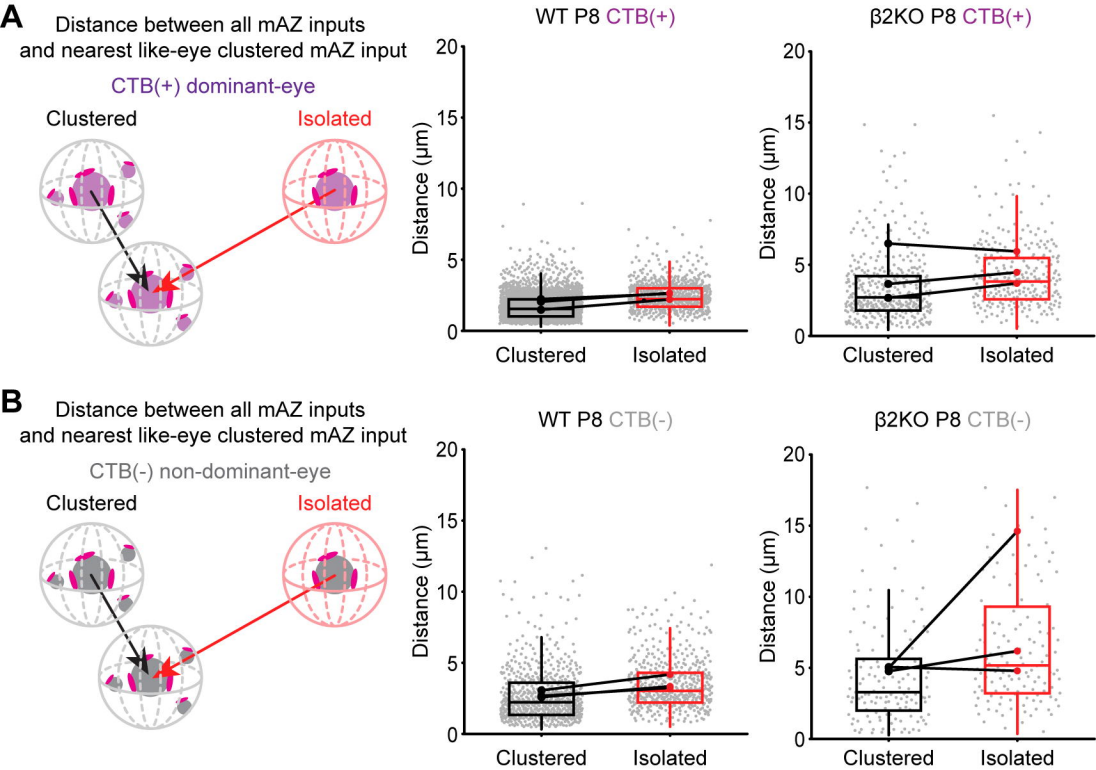
A
Distance between all mAZ inputs
and nearest like-eye clustered mAZ input
CTB(+) dominant-eye
Clustered
Isolated
WT P8 CTB(+)
β2KO P8 CTB(+)
Distance (µm)
0
5
10
15
20
Clustered
Isolated
B
Distance between all mAZ inputs
and nearest like-eye clustered mAZ input
CTB(-) non-dominant-eye
Clustered
Isolated
WT P8 CTB(-)
β2KO P8 CTB(-)
Distance (µm)
0
5
10
15
20
Clustered
Isolated

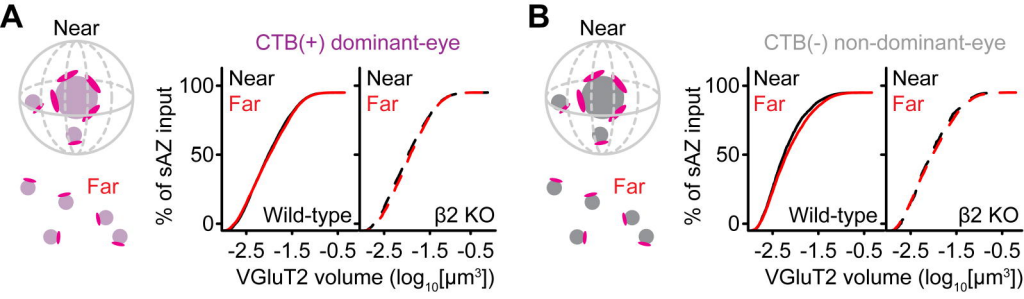
A
Near
Far
CTB(+) dominant-eye
% of sAZ input
100
50
0
Near
Far
Wild-type
β2 KO
-2.5 -1.5 -0.5 -2.5 -1.5 -0.5
VGluT2 volume (log10[μm3])
B
Near
Far
CTB(-) non-dominant-eye
% of sAZ input
100
50
0
Near
Far
Wild-type
β2 KO
-2.5 -1.5 -0.5 -2.5 -1.5 -0.5
VGluT2 volume (log10[μm3])